Materials & Design 266 (2026) 116184

Contents lists available at ScienceDirect

Materials & Design

journal homepage: www.elsevier.com/locate/matdes

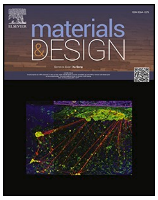

Optimum scandium addition in A356 cast alloys: alloy design, microstructural evolution and mechanical properties

Priyansh Khandelwal [a], Raluca Florentina Negrea [a], Jason Nunn [b], Scott Honan [c], Shouxun Ji [a,*]

[a] *Brunel Centre for Advanced Solidification Technology (BCAST), Brunel University of London, Uxbridge UB8 3PH, United Kingdom*
[b] *NioCorp Technologies Limited, 3rd Floor 86 - 90 Paul Street, London EC2A 4NE, England, United Kingdom*
[c] *NioCorp Developments Ltd., 7000 South Yosemite, Suite 115, Centennial 80122, CO, USA*

ARTICLE INFO

Keywords:
Aluminium alloys
Casting
Microstructures
Mechanical properties
Strengthening Mechanism
Scandium addition

ABSTRACT

The effect of scandium (Sc) addition on the microstructural evolution and mechanical properties of A356.2 cast alloys in both as-cast and T6 heat-treated conditions was investigated using a combined thermodynamic and experimental approach to identify an optimum composition for enhanced performance. Thermodynamic calculations and cooling curve analysis showed that Sc alters solidification behaviour through the formation sequence of Sc-containing intermetallic phases. Experimental results demonstrated that Sc additions up to 0.4 wt % significantly refined primary α-Al grains and reduced secondary dendrite arm spacing (SDAS), while modifying eutectic Si from coarse plate-like to fine fibrous morphology. The transformation of β-Al_5FeSi into compact Al-Fe-Si-Sc phases and the formation of nanoscale Al-Si-Sc-(Ti) dispersoids further contributed to strengthening. In the as-cast condition, the A356-0.4Sc alloy exhibited the best combination of strength and ductility, whereas under T6 heat treatment, the A356-0.2Sc alloy showed superior performance due to enhanced precipitation strengthening and thermal stability of Sc-containing dispersoids. At higher Sc content (0.6 wt%), primary $AlSc_2Si_2$ formation led to microstructural coarsening and reduced properties. This study establishes an optimum Sc addition range of 0.2–0.4 wt% and provides mechanistic insight into the role of Sc in alloy design.

1. Introduction

Al-Si-Mg casting alloys such as A356 and A357 are commonly used in automotive and aerospace industries due to their excellent castability, corrosion resistance, and balanced mechanical properties. These alloys are used to make various parts, such as structural components, wheels and aircraft housings, where weight reduction, fatigue resistance and stability are critical [1,2]. However, the conventional A356 alloys have various limitations, including coarse primary α-Al dendrites, large secondary dendrite arm spacing (SDAS), acicular eutectic silicon and brittle Fe-rich intermetallic compounds. All these microstructural features act as stress concentrators and limit ductility and fatigue performance, especially under dynamic or thermal loading conditions [3].

To overcome these challenges, a range of chemical modification strategies have been developed over the past decades. Grain refiners such as Ti, B, Nb, and Zr are typically introduced in the form of Al-Ti-B, Al-Ti-C or Al-Nb-B master alloys to refine primary α-Al grains [4–7]. Their effectiveness arises from the presence of TiB_2/Al_3Ti particles, which serve as potent heterogeneous nucleation sites [8,9]. Similarly, eutectic modifiers such as Sr, Na, Sb, and Ca are used to alter the morphology of eutectic Si from coarse plate-like to fine fibrous structures by impurity induced twining (IIT) or poisoning of the twin-plane re-entrant edge (TPRE) mechanisms, which are well explained in literature [10–13]. Furthermore, Fe-phase modifiers such as Mn, Co, and Cr are often used to counter the detrimental β-Al_5FeSi intermetallics by converting them into less harmful α-$Al_{15}(Fe, Mn)_3Si_2$ or π-$Al_8FeMg_3Si_6$ phases [14–16].

Although these additions have proven effective in improving specific microstructural aspects, they also present significant drawbacks. Conventional grain refiners such as Al-Ti-B suffer from fading effects during prolonged melt holding due to the agglomeration or sedimentation of TiB_2 particles and the formation of Al_3Ti films that poison nucleation sites [17,18]. Eutectic modifiers like Sr and Na are also prone to oxidation and porosity formation, making their modification effect transient and process sensitive [19,20]. Similarly, excessive additions of Fe modifiers such as Mn and Cr can promote the formation of sludge-

---

[*] Corresponding author.
E-mail address: Shouxun.Ji@brunel.ac.uk (S. Ji).

https://doi.org/10.1016/j.matdes.2026.116184
Received 28 February 2026; Received in revised form 27 April 2026; Accepted 5 May 2026

type intermetallics, thus affecting castability and mechanical properties [21]. More importantly, these modifiers tend to act independently, addressing only one microstructural feature (grain, eutectic, or Fe-phase) without improving the overall alloy system.

Considering these limitations, increasing attention has been directed toward rare-earth (RE) and transition-metal additions, such as cerium (Ce), yttrium (Y), lanthanum (La), zirconium (Zr), erbium (Er) and scandium (Sc), which have shown the potential to simultaneously refine grains whilst also modifying eutectic Si, and other intermetallic phases. These elements exhibit a strong chemical affinity for aluminium (Al), forming thermally stable Al-RE intermetallics that can act as heterogeneous nucleation sites during solidification and as strengthening precipitates during the subsequent heat treatment [22,23]. Among these elements, Sc has emerged as the most potent and multifunctional alloying addition. It forms coherent Al_3Sc dispersoids that act as potent heterogeneous nucleation sites during solidification, resulting in refined grains and during ageing, these dispersoids contribute significantly to precipitation strengthening. [24,25].

Despite these benefits, the optimum Sc content required to maximise microstructural refinement and mechanical performance in cast aluminium alloys remains unclear. A review of the literature (see Table 1 in Supplementary Material) shows significant variation in the reported optimum Sc content, typically ranging from 0.1 to 0.81 wt%. This variation depends on several factors, including alloy composition (e.g. A356, A357), processing route (e.g. gravity die casting, additive manufacturing), cooling rate, heat treatment conditions, and the presence of additional alloying elements such as Ti, Zr, Sr, and Cu. The lack of a consistent, integrated approach in these studies, especially one combining thermodynamic modelling with comprehensive experimental validation has contributed to the existing ambiguity.

The present work addresses these gaps by systematically investigating the role of Sc in A356.2 cast alloys using an integrated CALPHAD-experimental approach. Thermodynamic simulations (Scheil-Gulliver and equilibrium analyses) are first used to predict phase formation, freezing range, and overall changes in the solidification path with Sc addition. These predictions are then experimentally validated using differential scanning calorimetry (DSC), thermal analysis (cooling curves) and detailed microstructural characterisation (OM, SEM, TEM, and XRD). The resulting microstructural observations are correlated with mechanical properties in both as-cast and T6 heat-treated conditions to determine the optimum Sc concentration. This integrated approach aims to resolve the inconsistencies in literature by establishing a well-defined Sc addition range that provides the best balance of grain refinement, eutectic modification, and mechanical properties, while avoiding the formation of coarser, brittle Sc-rich intermetallics.

2. Materials and Methods

2.1. Alloy Design- thermodynamic calculations (CALPHAD)

To guide alloy selection and processing parameters, thermodynamic simulations were done using the CALPHAD approach in Thermo-Calc® 20203b software (TCAL8 database). Equilibrium phase diagrams and Scheil solidification curves for the Al-Si-Mg-Sc system were calculated to evaluate the solidification sequence, phase stability, and the onset of intermetallic phase formation. These calculations helped determine processing windows and critical Sc concentrations beyond which coarse $AlSc_2Si_2$ phases might precipitate.

Table 1
Chemical composition of the experimental A356.2-Sc alloys measured by optical emission spectroscopy (OES), wt.%.

Alloy name	Al	Si	Mg	Fe	Sc	Ti
Baseline	Bal.	6.96	0.33	0.11	–	0.12
0.2 Sc	Bal.	7.14	0.31	0.10	0.21	0.10
0.4 Sc	Bal.	7.27	0.31	0.09	0.41	0.09
0.6 Sc	Bal.	7.34	0.30	0.10	0.62	0.09

2.2. Alloy Preparation

Commercial A356.2 alloy was used as the baseline material for this study with a nominal composition as shown in Table 1. Three experimental alloys were prepared by adding Sc in the form of an Al-2 wt% Sc master alloy to achieve target compositions of 0.2, 0.4 and 0.6 wt% Sc, in addition to the baseline A356.2 alloy. Alloys were melted in an electric resistance furnace using a graphite-SiC crucible at 760 °C and was held till the melt was homogenised. The temperature of the melt was checked using a K-type thermocouple. To compensate for the dilution of Si and Mg due to the addition of Al-2Sc during melting, controlled additions of Al-20Si and Al-25 Mg master alloys were made to restore the nominal alloy chemistry. The melt was covered with a commercial granular flux and then the melt was subjected to degassing, during which high-purity argon was blown into the melt by using a rotary degasser at a rotating speed of 300 rpm and gas pressure of 6 l/min for 6–8 min. Dross was skimmed and the melt was held until it reached to a temperature of 725 °C. Hydrogen porosity and melt cleanliness were assessed using the Density Index (DI), which was measured using an IDECO hydrogen analyser with double sample crucibles under vacuum and atmospheric pressure. Simultaneously, cooling curve analysis was carried out on the IDECO thermal analysis system by placing a thermocouple in the centre of a cylindrical sample cup. The temperature–time data were recorded during solidification, and the cooling rate curves were obtained by calculating the rate of temperature change with time. It was ensured that the DI was less than 1%. Thereafter, the melt was poured at 720 ± 5 °C in BS L101 permanent steel moulds preheated at 200 °C to obtain cylindrical samples of 20 mm diameter and 150 mm length, which were then machined to get tensile samples according to the ASTM E8 standard [26] as shown in Fig. 1.

2.3. Heat treatment

To determine the optimal solutionising parameters for maximising mechanical properties, heat treatment trials were carried out at multiple temperatures and durations. Samples were solution treated at 535 °C, and 540 °C for various durations ranging from 7 to 8 h. After solution treatment, samples were immediately quenched in water to room temperature. Subsequently, artificial ageing was performed at 170 °C for 8 h. These heat treatment conditions were chosen to identify the optimum combination yielding maximum hardness, ensuring optimal precipitation of strengthening phases. The optimised parameters obtained from these trials were then used for all further mechanical property evaluations and microstructural characterisations.

2.4. Microstructure and phase composition characterization

For microstructural analysis, samples were sectioned from the tensile bar gauge length, ground using SiC papers, and polished with a 0.05 μm SiO_2 suspension. Electrochemical etching using Barker's reagent (200 mL H_2O + 10 mL 35% fluoroboric acid) was applied to reveal grain boundaries. Polarized light microscopy was conducted using a Zeiss Scope A1, and quantitative image analysis was performed using ImageJ. Scanning Electron Microscopy (SEM) and Energy Dispersive X-ray Spectroscopy (EDS) were conducted using a Crossbeam 340 FEG SEM-FIB operating at 15 kV. For nanostructural characterization, Transmission Electron Microscopy (TEM) was performed using a Spectra 300 from ThermoFisher operated at 200 kV and equipped with a Super-X EDS detector for chemical analysis. TEM samples were prepared by mechanical thinning to < 150 μm thickness, followed by punching 3 mm diameter discs. Electron transparency was achieved by precision ion polishing using a Gatan PIPS II system. For phase identification, X-ray diffraction (XRD) performed using a Bruker D8 Advance X-Ray

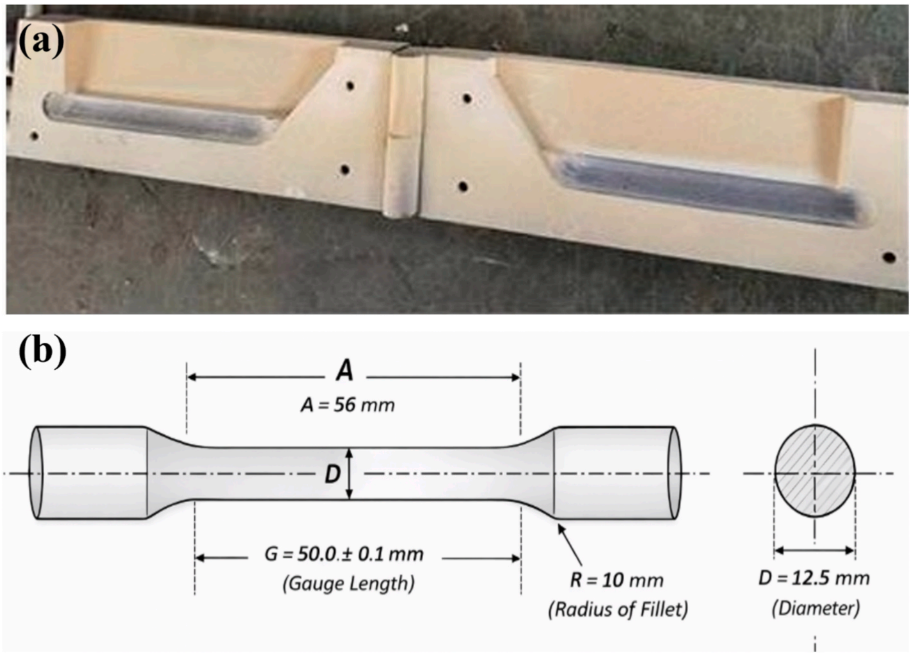

Fig. 1. (a) BS L101 permanent steel mould, (b) tensile specimen machined from the BS L101 mould according to ASTM E8 standard.

diffractometer and phase transformation behaviour was studied using a Netzsch STA 409 PC Differential Scanning Calorimetry (DSC).

2.5. *Mechanical properties*

The Tensile testing was performed using an Instron 5892 universal electromechanical testing machine equipped with Bluehill software. Tests were conducted according to ASTM E8/E8M standards with specimens machined from the cast bars having a gauge length of 50 mm and gauge diameter of 12.5 mm. Each reported result represents the average of 5 specimens. An extensometer with a gauge length of 50 mm, and the strain rate of 1 mm/min was used to ensure precise strain measurements. The yield strength (0.2% offset), ultimate tensile strength (UTS), and elongation to fracture were recorded. Vickers hardness measurements were performed on polished specimens using a load of 1 kg and a dwell time of 10 s on a ZHVμ-Semi Micro Vickers Hardness Tester. At least 7 readings were taken for each sample to ensure statistical reliability.

3. Results

3.1. *Thermodynamic solidification behaviour*

The Scheil-Gulliver solidification model and equilibrium phase-fraction analysis in Thermo-Calc® 2023b using the TCAL8 database were used to perform thermodynamic simulations for the A356.2 baseline alloy and Sc-modified compositions (A356-0.2Sc, A356-0.4Sc, and A356-0.6Sc). The typical actual castings were replicated using the Scheil model under non-equilibrium conditions, which assume complete mixing in the liquid and no diffusion in the solid phase. The solidification sequence, phase transformations, and temperature ranges controlling microstructural evolution in the Sc-modified A356 alloys are all explained comprehensively by these computations.

Fig. 2 displays the simulated Scheil solidification curves for each of the four alloys, while the corresponding phase-fraction evolution plots are shown in Fig. 3. According to these curves, the baseline A356.2 alloy starts to solidify when primary α-Al (FCC) nucleates at about 615.20 °C, followed by the solidification of Si at about 574.82 °C and Mg_2Si at about 558.66 °C with solidification completed at about 558.63 °C. About 92–93% of the solid fraction is made up of the primary α-Al phase, with Si and Mg_2Si appearing later to form the eutectic structure characteristic of Al-Si-Mg alloys.

The solidification sequence is considerably altered after alloying with Sc, but the overall solidification temperature range stays almost unchanged. At about 570 °C, a new ternary phase, $AlSc_2Si_2$ appears for the A356-0.2Sc alloy. In the later phases of solidification, this phase coexists with α-Al and Si, suggesting that Sc has strong interactions with both Al and Si. $AlSc_2Si_2$ formation can inhibit the growth of coarse eutectic Si and encourage finer microstructures by slightly lowering the Si fraction in the liquid from 7.5% in the baseline alloy to 6.7%. The simulations also indicate the formation of a small quantity (0.2%) of the $AlSc_2Si_2$ intermetallic phase. This phase forms toward the end of solidification. Its limited fraction means that only a small portion of Si is consumed in forming $AlSc_2Si_2$, leaving adequate Mg and Si available to form Mg_2Si during solidification and subsequent ageing. In the A356-0.4Sc alloy, the formation temperature of $AlSc_2Si_2$ shifts slightly upward to 571.75 °C, and it contributes to around 0.61% of the total solidification fraction, as observed from its persistence down to the end of solidification. The overall Si after complete solidification is around 6.3% of the total fraction. At 0.6 wt% Sc, the $AlSc_2Si_2$ phase becomes more thermodynamically stable, forming over a wider temperature range as it starts to solidify from 582.14 °C and remains persistent through the final stages of solidification, contributing to around 0.91% of the total solidification phases. As a result, the total Si reduces to 6.1%. Interestingly, as solidification progresses, $AlSc_2Si_2$ continues to grow simultaneously along with α-Al, leading to interpenetrating morphologies or blocky $AlSc_2Si_2$ particles within the α-Al matrix.

The enhanced formation of $AlSc_2Si_2$ consumes more Si from the liquid and the matrix, thereby reducing the Si that can enter solid solution during solution treatment, which in turn decreases the number density of Mg_2Si precipitates formed during ageing. Furthermore, the $AlSc_2Si_2$ particles formed at higher Sc levels are coarse, stable, and largely stable during heat treatment. These intermetallics do not dissolve or re-precipitate during ageing and therefore do not contribute to strengthening. On the contrary, they may reduce ductility and ultimate tensile strength marginally by acting as stress concentrators under load. A summary of the phase transformation temperatures and solidification reactions predicted for all compositions is presented in Table 2.

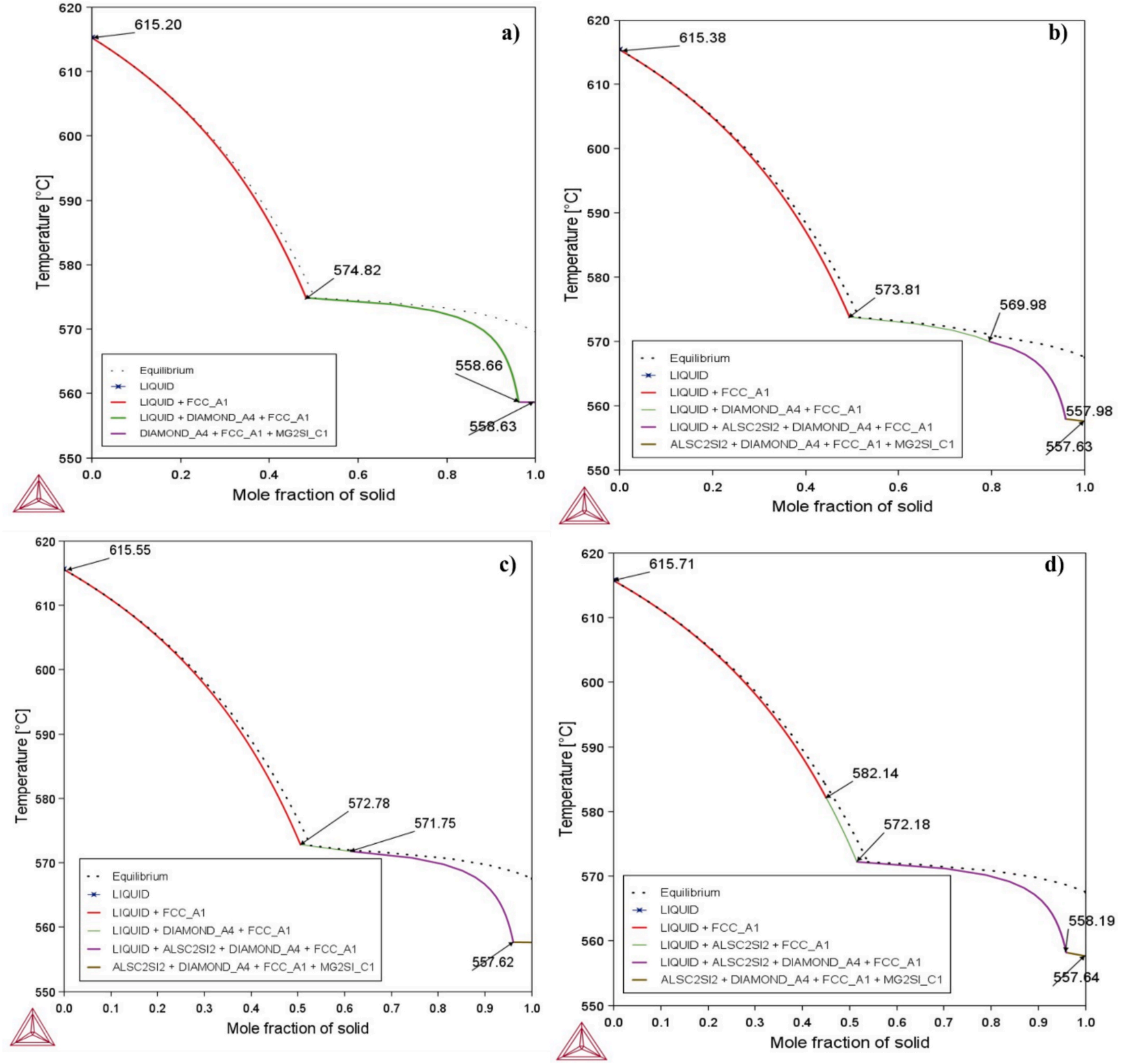

Fig. 2. Scheil solidification curves for (a) A356.2, (b) A356-0.2Sc, (c) A356-0.4Sc, and (d) A356-0.6Sc alloys simulated using Thermo-Calc.

3.2. *Differential scanning calorimetry (DSC) analysis*

The solidification and melting behaviour of A356.2 and A356-Sc alloys were evaluated using DSC, and the corresponding thermograms are shown in Fig. 4. The curves have two major endothermic peaks corresponding to the primary α-Al solidification and the Al-Si eutectic reaction, and a small peak near 560 °C. The thermal parameters determined from the DSC curves are summarised in Table 3.

In the case of the A356.2 alloy, the peak for the primary α-Al occurs at a temperature of 616.7 °C, corresponding to the liquidus temperature, followed by a eutectic transformation occurring at 587.8 °C, and finally, the solidus temperature occurs at 558.8 °C. Upon adding Sc, a refinement of thermal behaviour is observed for all alloys. The liquidus temperature for all alloys remains relatively unchanged, indicating that adding Sc has little effect on the solidification temperature for these alloys. However, a small decrease in the eutectic and solidus temperatures is noticeable for the A356-0.2Sc and A356-0.4Sc alloys, reaching 584.6 °C and 584.2 °C, respectively. This drop in eutectic temperature can be attributed to the modification of the Si phase and the formation of minor Sc-containing intermetallics ($AlSc_2Si_2$), which locally delay eutectic nucleation by consuming Si from the melt. For A356-0.6Sc, the eutectic temperature increases marginally to 584.9 °C, accompanied by a minor rise in the solidus temperature to 557.1 °C. This behaviour correlates well with Thermo-Calc predictions, which show that $AlSc_2Si_2$ begins to solidify earlier along with α-Al and persists until the final stages of solidification alongside α-Al, Si and Mg_2Si. Additionally, a minor endothermic peak observed near 558.5–560 °C is associated with the transformation of secondary phases such as Mg_2Si and $AlSc_2Si_2$. These phases form during the final stages of solidification and dissolve upon reheating.

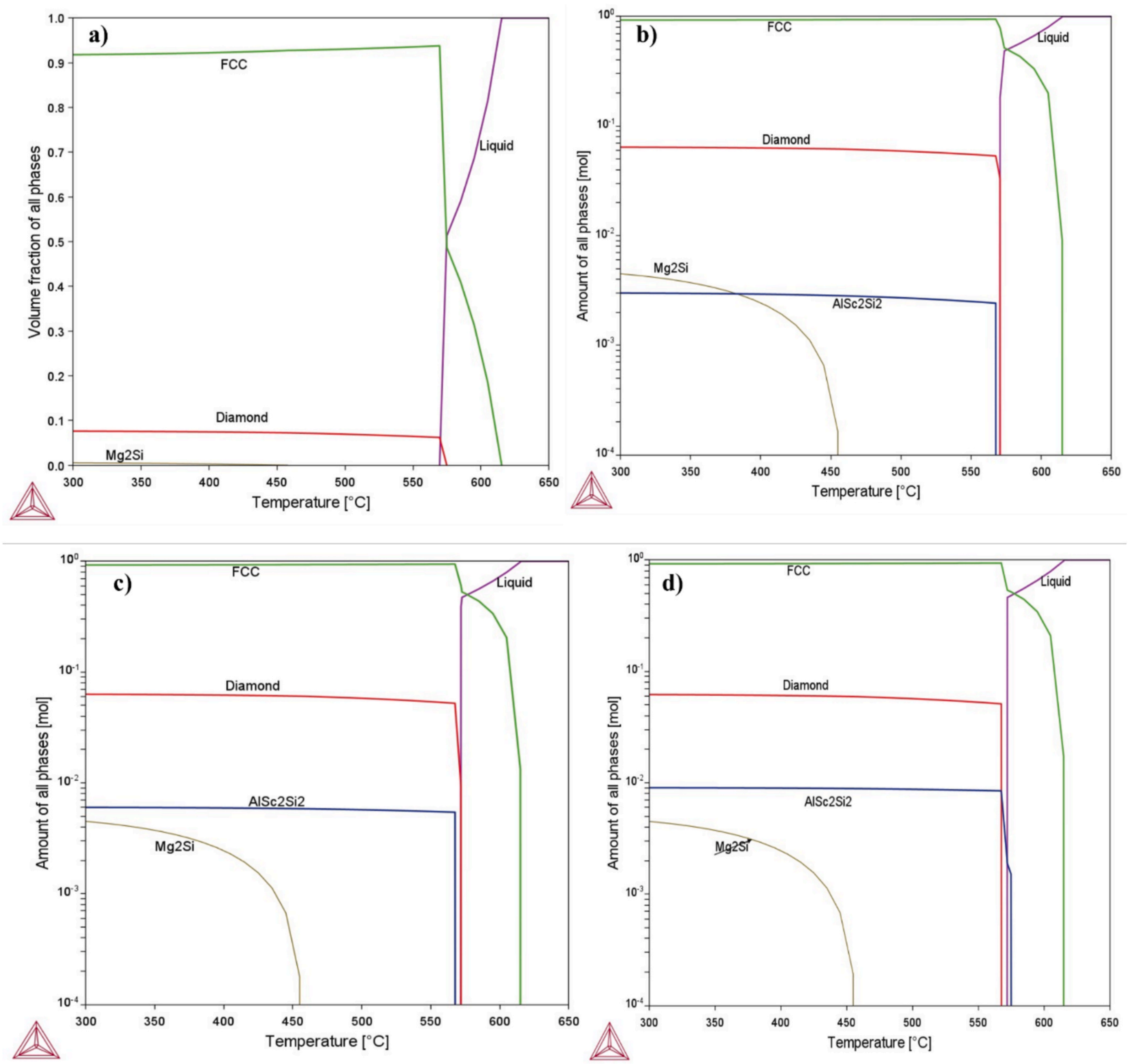

Fig. 3. Phase fraction evolution of (a) A356.2, (b) A356-0.2Sc, (c) A356-0.4Sc, and (d) A356-0.6Sc alloys during solidification.

Table 2
Phase transformation temperatures and solidification reactions predicted by Thermo-Calc Scheil simulations.

Alloy	Liquidus (°C)	Onset of Si (°C)	$AlSc_2Si_2$ Formation (°C)	Mg_2Si Formation (°C)	Solidus (°C)	Solidification Reactions
A356	615.20	574.82	—	558.66	558.63	L → α-Al L → α-Al + Si L → α-Al + Si + Mg_2Si
A356-0.2Sc	615.38	573.81	569.98	557.98	557.63	L → α −Al L → α −Al + Si L → $AlSc_2Si_2$ + Si + α −Al L → α −Al + $AlSc_2Si_2$ + Si + Mg_2Si
A356-0.4Sc	615.55	572.78	571.75	557.62	557.60	L → α −Al L → α −Al + Si L → $AlSc_2Si_2$ + Si + α −Al L → α −Al + $AlSc_2Si_2$ + Si + Mg_2Si
A356-0.6Sc	615.71	572.18	582.14	558.19	557.64	L → α −Al L → $AlSc_2Si_2$ + α −Al L → α −Al + $AlSc_2Si_2$ + Si L → α −Al + $AlSc_2Si_2$ + Si + Mg_2Si

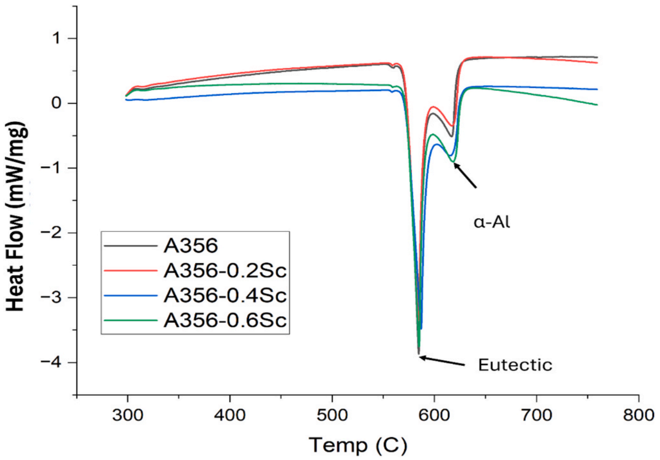

Fig. 4. DSC thermograms of A356.2 and A356-Sc alloys showing α-Al and eutectic peaks.

Table 3
Thermal characteristics determined from DSC for A356.2 and A356-Sc alloys.

Alloy	Liquidus Temperature (°C)	Eutectic Peak Temperature (°C)	Eutectic Onset Temperature (°C)	Solidus Temperature (°C)
A356.2	616.7	587.8	573.1	558.8
A356-0.2Sc	616.1	584.6	571.9	556.8
A356-0.4Sc	614.7	584.2	571.1	556.1
A356-0.6Sc	618.6	584.9	572.2	557.1

3.3. Microstructure of the alloys: SDAS, grain size, modification of eutectic Si and Fe-bearing intermetallic

Fig. 5 shows the optical micrographs of A356.2 alloy with and without Sc, where it is clear that there is a difference in grain size and eutectic Si morphologies. The microstructure of the baseline A356.2 alloy shows a typical dendritic microstructure consisting of primary α-Al dendrites surrounded by a network of acicular, plate-like eutectic Si particles. The average α-Al grain size of this alloy was 540 ± 39 μm. With the addition of Sc, substantial microstructural refinement was observed. The A356-0.2Sc alloy showed the formation of uniformly distributed equiaxed grains, with reduced grain size to 338 ± 26 μm. In addition, the eutectic Si appeared more fragmented and rounded compared to the unmodified alloy. Further refinement occurred at 0.4 wt% Sc, where the α-Al grains were the finest, i.e., 260 ± 22 μm and the eutectic Si showed a well-modified fibrous morphology. However, the A356-0.6Sc alloy showed limited refinement; instead, local coarsening and segregation of Sc-rich intermetallics occurred, slightly increasing the average grain size to 413 ± 24 μm. Partial coarsening of Si is also observed for this alloy, likely due to the early formation of Sc-Si containing intermetallic compounds that consume Si from the melt, thereby reducing the availability of Si during the eutectic transformation.

A similar pattern was observed with the SDAS as it decreased systematically from 24.10 ± 3.05 μm in the baseline alloy to 22.55 ± 2.24 μm at 0.2 wt% Sc, 19.73 ± 1.94 at 0.4 wt% Sc. This reduction reflects enhanced nucleation rates and suppressed dendrite growth due to Sc solute redistribution and local thermal gradients during solidification. For the A356-0.6Sc alloy, the SDAS increases to 22.45 ± 1.82. This indicates a critical threshold for effective Si modification before Sc saturation and phase segregation occur.

Fig. 6 shows the XRD profiles of A356.2 and Sc modified A356 alloys. It is observed that β-Al5FeSi and π-Al8$Mg_3Si_6Fe_1$ phases were present in all the alloys, whereas the alloys containing Sc have several extra peaks corresponding to the Sc-containing $AlSc_2Si_2$ phase.

Fig. 7 compares the backscattered electron (BSE) microstructures of

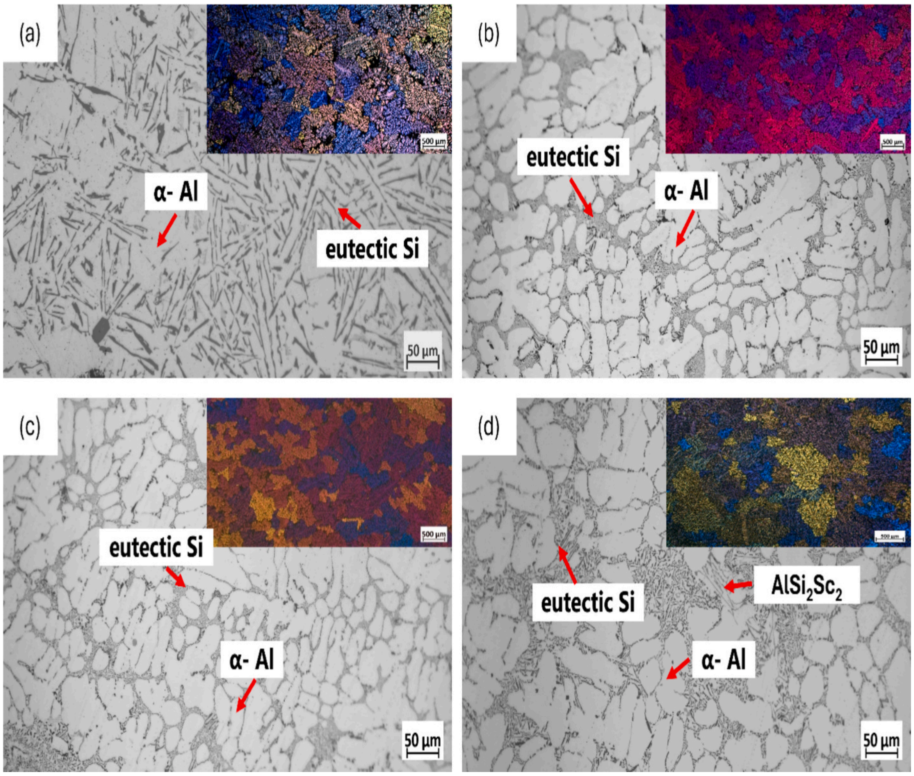

Fig. 5. Optical Micrographs showing the grains and eutectic Si in (a) A356.2; (b) A356-0.2Sc; (c) A356-0.4Sc; (d) A356-0.6Sc alloys in as-cast condition.

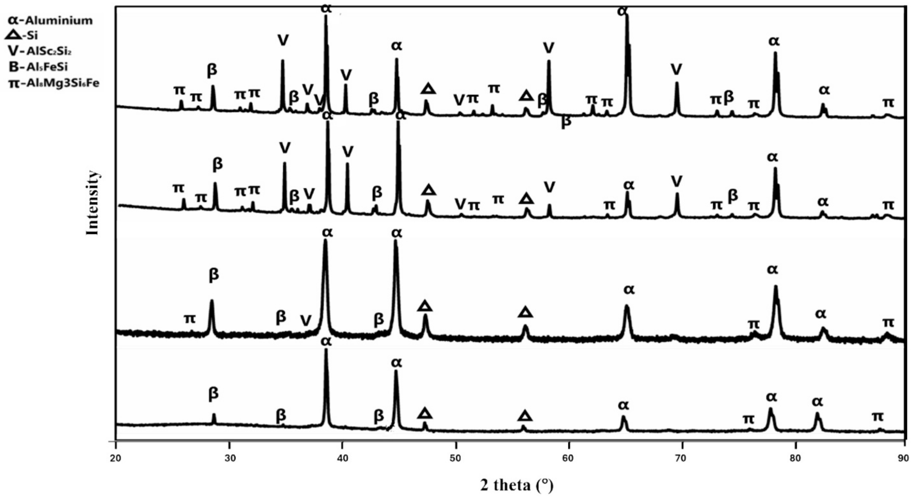

Fig. 6. The XRD spectrum of as-cast A356.2, A356-0.2Sc, A356-0.4Sc and A356-0.6Sc alloys.

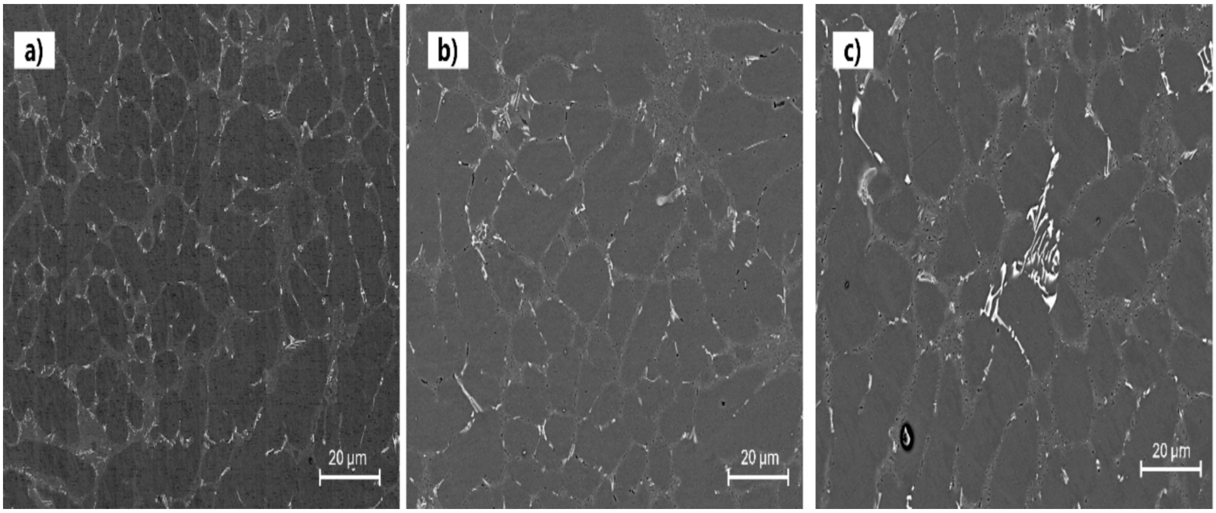

Fig. 7. BSE images highlighting the distribution of Sc-rich intermetallics (bright contrast) in (a) A356-0.2Sc, (b) A356-0.4Sc and (c) A356-0.6Sc alloys.

the A356-0.2Sc (Fig. 7(a)), A356-0.4Sc (Fig. 7(b)) and A356-0.6Sc (Fig. 7(c)) alloys. The bright contrast regions correspond to Sc- and Fe-rich intermetallic phases, while the black matrix represents the α-Al phase. In the alloys containing 0.2Sc and 0.4Sc, the presence of fine, uniformly distributed bright intermetallics is observed primarily in the interdendritic regions. These are identified as $AlSc_2Si_2$ intermetallic phases that form along with Si during the latter stages of solidification. The fine and homogeneous distribution of these phases indicate effective solute partitioning behaviour of Sc and controlled nucleation of $AlSc_2Si_2$ within the eutectic regions. In contrast, in the A356-0.6Sc alloy, the intermetallics have a coarse and more clustered morphology in the interdendritic regions and along the α- Al grains. The increase in Sc concentration in the alloy causes the formation and growth of $AlSc_2Si_2$ phases at an early stage in the solidification process, which coarsens due to solute supersaturation and the limited diffusion of Sc at high concentrations. This causes a certain degree of coalescence in the Sc-containing phases.

Fig. 8 (a), (b) and (c) shows the SEM micrographs and EDS spectrum of the A356-0.2Sc alloy, where the morphology and chemical composition of Fe-rich and $AlSc_2Si_2$ intermetallics are presented. The Fe-bearing phases in the A356 alloy are found to be predominantly of the β-Al_5FeSi type, which have a long plate-like or needle-like morphology and are present along the interdendritic regions, as shown in Fig. 8(d). These acicular β-phase intermetallics are known to adversely affect the ductility and fatigue properties. The presence of Sc in the A356 alloy causes a significant modification in the morphology and distribution of Fe-rich intermetallics. For 0.2 to 0.4 wt% Sc, the plates of the β-phase intermetallics are found to be compact and shorter, transforming to an irregular or nodular shape. The modification in the Fe-rich intermetallics is attributed to the strong interaction between Sc, Fe, and Si, resulting in the nucleation of complex (Al, Fe, Si, Sc) compounds with a rounded and nodular shape.

Fig. 9 shows the phase maps of the A356-0.4Sc alloy, indicating the coexistence of Sc and Fe containing intermetallic compounds in the interdendritic regions. The primary Sc-containing phase was found to be $AlSc_2Si_2$, which occurred mostly in the form of faceted compact network-like particles, usually at the α-Al dendrite boundaries. This morphology represents the equilibrium growth form of $AlSc_2Si_2$, as reported for Sc-containing Al-Si alloys. The point analysis of the bright contrast area using EDS confirmed the presence of a stoichiometric $AlSc_2Si_2$ phase with a composition of around 46.3 at. % Al, 27.1 at. % Si, and 23.1 at. % Sc, with minor enrichments of Mg, as presented in Table 4.

In addition to the above phase, Fe-rich intermetallics were also detected, which include AlFeSiMg and AlFeMgScSi compounds. These compounds have an elongated platelet or irregular Chinese-script

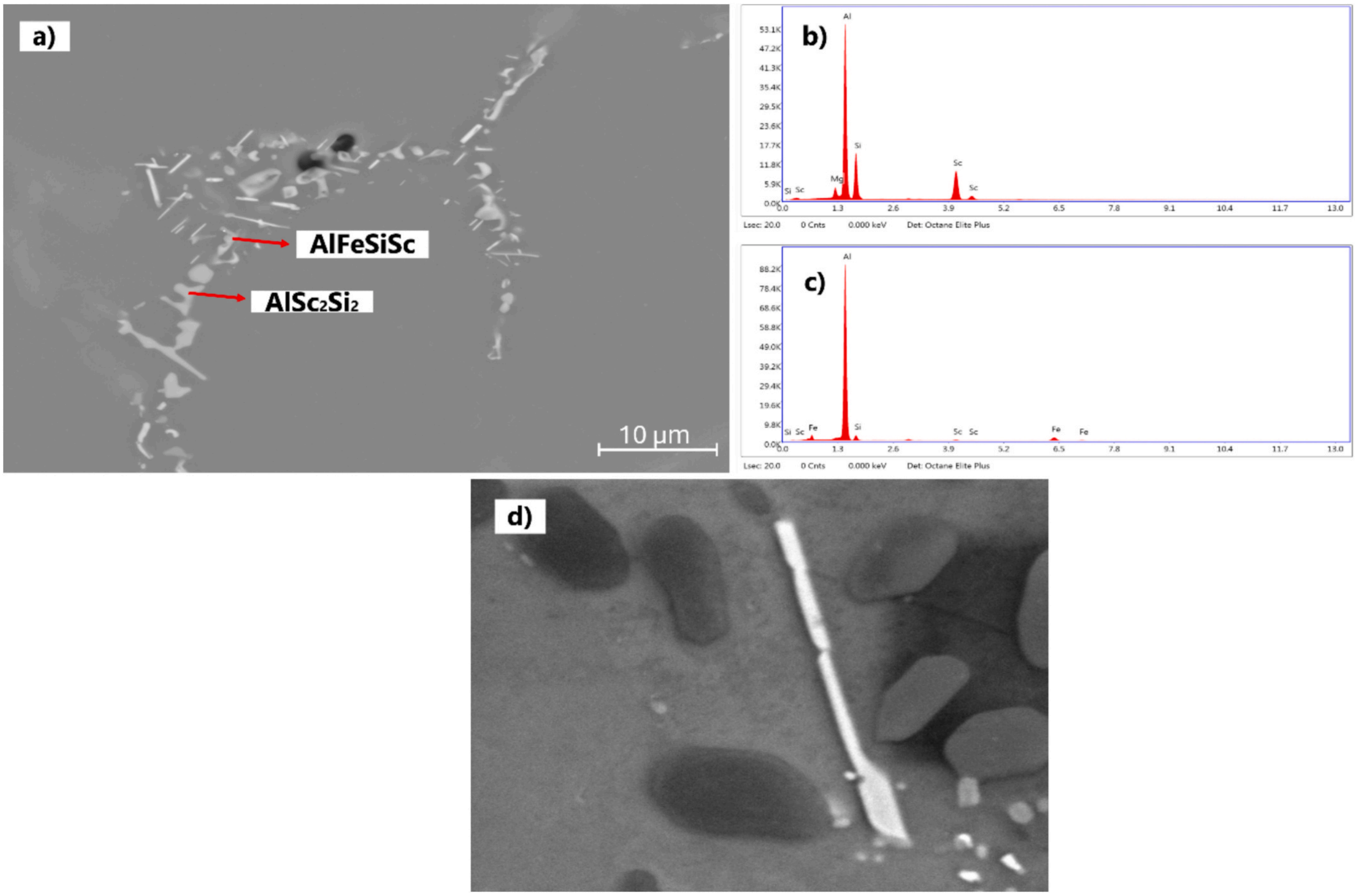

Fig. 8. SEM images illustrating: (a) morphological evolution of Fe-rich intermetallics and AlSc2Si2 in A356-0.2Sc alloy; (b) EDS spectrum of Fe intermetallic; (c) EDS spectrum of AlSc2Si2; and (d) needle-like Fe intermetallic in baseline A356.2 alloy.

morphology. The composition of these phases, as listed in Table 4, shows a partial substitution of Fe and Mg in the Al-Si-Sc matrix with a Sc content of up to 4 at. % in the Fe-rich phases. The detection of AlFeMgScSi phases indicates a partial interaction between Fe-containing and Sc-containing phases, which can further refine the morphology of Fe intermetallics by modifying the local Fe/Si ratio during solidification.

In addition to the dominant blocky $AlSc_2Si_2$ morphology, a small fraction of the alloy exhibited a hollow frame-like morphology as shown in Fig. 10. These frame-type morphologies are rarely reported in Al-Si-Sc systems but likely arise under diffusion-limited, non-equilibrium conditions. During the final stages of solidification, localised Sc and Si enrichment in the residual liquid can lead to solute supersaturation and constitutional undercooling, destabilising the solid–liquid interface and promoting anisotropic growth. The low diffusivity of Sc in liquid Al promotes this effect, resulting in the open, branched growth front observed. Similar eutectic morphologies were also reported for the microstructure of Mg-Sn-Al-Zn-Mn alloys [27], where the eutectic Mg_2Sn and Al-Mn-Sn compounds developed open or interconnected networks under diffusion-controlled solidification. In that study, like the current investigation, the irregular eutectic morphology was related to the solute-enriched liquid layers ahead of the solid–liquid interface, which resulted in anisotropic growth. Guo et al. [28] observed similar morphology in an Al-7Si-1.5Sc alloy. According to this study, the hollow rhombi $AlSc_2Si_2$ phase may precipitate by the peritectic reaction $L + Al_3Sc \rightarrow AlSc_2Si_2$ at 898 K, whereas the typical network-like $AlSc_2Si_2$ phase may precipitate by the eutectic reaction $L \rightarrow AlSc_2Si_2 + Si + \alpha - Al$ at 844 K.

3.4. Mechanical properties

Fig. 11(a) shows the variation of Vickers hardness of the A356.2 and Sc-modified alloys in the as-cast condition. The Vickers hardness values showed a steady rise with the Sc addition of up to 0.4 wt%. The baseline A356.2 alloy had a hardness of 62.77 HV, which increased to 68.67 HV in the A356-0.2Sc alloy and further to a maximum of 71.53 HV in the A356-0.4Sc alloy. However, this increase in hardness was less pronounced at higher Sc content, where the hardness of the A356-0.6Sc alloy was 65.97 HV.

Fig. 11(b) demonstrates the variation of Vickers hardness for all the alloys in T6 heat treatment conditions. For the A356.2 and A356-0.2Sc alloys, the optimum heat treatment conditions have been determined as solution treatment at 540 °C for 8 h and artificial ageing at 170 °C for 8 h. Under these conditions, the hardness values were 109.45 HV for the A356 and 112.12 HV for the A356-0.2Sc. However, when the same heat treatment parameters were used for the A356-0.4Sc and A356-0.6Sc alloys, the increase in hardness values was less pronounced, as can be seen for A356-0.4Sc-T6a, where a hardness of 107.34 HV was recorded. Therefore, the solution treatment temperature and time were reduced to 535 °C for 7 h and ageing at 170 °C for 8 h and 9 h, respectively, for the A356-0.4Sc and A356-0.6Sc alloys. In this case, the A356-0.4Sc alloy showed hardness values of 108.83 HV, whereas the A356-0.6Sc alloy had a hardness of 105.45 HV.

Fig. 12 (a) shows the tensile properties of A356.2 and Sc-modified A356 alloys in the as-cast condition. The yield strength (YS), ultimate tensile strength (UTS), and elongation increased consistently with the addition of Sc up to 0.4 wt%. The baseline A356.2 alloy had YS of 106.46 MPa, UTS of 179.26 MPa, and elongation of 3.94%. With the

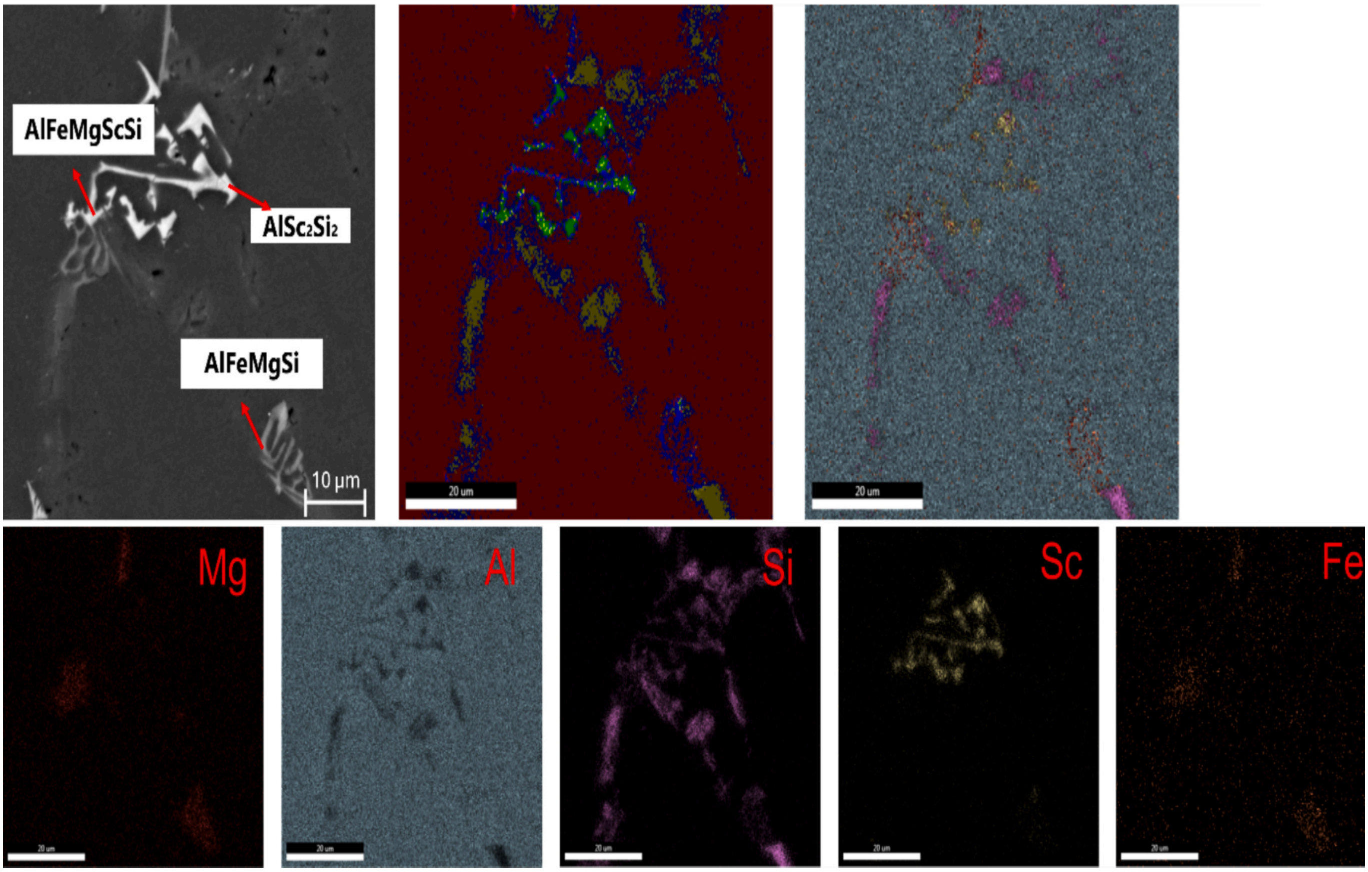

Fig. 9. Phase map of A356-0.4Sc alloy showing $AlSc_2Si_2$ (bright regions) and Fe-bearing intermetallics (AlFeMgScSi and AlFeMgSi).

Table 4
Chemical composition of various intermetallics present in A356-0.2Sc and A356-0.4Sc alloys using SEM-EDS analysis.

S. No.	Phase	Element (at. %)				
		Al	Si	Sc	Fe	Mg
1	$AlSc_2Si_2$	46.30	26.06	24.12	–	3.52
2	AlFeSiMgSc	47.84	26.87	4.01	4.56	16.81
3	AlFeSiMg	82.31	10.47	–	1.20	6.03
4	AlFeSiSc	80.21	11.64	2.63	5.52	–

addition of 0.2 wt% Sc, these values increased to 116.13 MPa, 207.77 MPa, and 6.17%, respectively. The maximum strength and ductility were obtained at 0.4 wt% Sc, where the alloy had YS of 122.65 MPa, UTS of 224.00 MPa, and elongation of 8.94%. Further addition of Sc to 0.6 wt % caused a slight reduction in YS and UTS to 111.17 MPa and 210.78 MPa, respectively, while elongation remained relatively high at 7.46%.

In the T6 heat-treated condition (Fig. 12 (b)), all alloys showed a substantial improvement in strength and ductility compared to the as-cast condition. The baseline A356.2-T6 alloy had YS of 252.98 MPa, UTS of 306.00 MPa, and elongation of 6.15%. Adding 0.2 wt% Sc to the alloy resulted in an increase in YS, UTS, and elongation to 261.12 MPa, 323.70 MPa, and 9.46%, respectively. For the A356-0.4Sc alloy, in the first heat treatment cycle (540 °C/8h solution + 170 °C/8h ageing), the YS and UTS were 250.33 MPa and 313.96 MPa, with an elongation of 7.22%. In the modified heat treatment cycle (535 °C/7h solution + 170 °C/8h ageing) was applied, the YS and UTS were 243.52 MPa and 319.45 MPa, with the elongation of 11.18%. For the A356-0.6Sc alloy, in the optimised heat treatment cycle (535 °C/7h + 170 °C/9h ageing), the tensile properties were 237.16 MPa YS, 308.56 MPa UTS, and 10.55% elongation. From the above results, it can be concluded that Sc addition up to 0.2 wt% is effective in enhancing strength and ductility in as-cast and T6 conditions, and 0.4 wt% Sc addition resulted in optimum mechanical properties in the as-cast condition and moderate properties in T6 condition. Whereas higher Sc levels of 0.6 wt% show less pronounced improvements in mechanical properties in the as-cast and a reduction in YS or less pronounced improvement in other properties under T6 conditions.

The mechanical properties obtained in this study are consistent with, and in some cases exceed, those reported in the literature for Sc-modified A356 alloys. For example, Xu et al. [29] reported a maximum UTS of 278 MPa in the T6 condition for A356 alloys modified with 0.35 wt% Sc, while elongation was only around 4.3%. Similarly, Masita et al. [30] reported a tensile strength of around 313 MPa for A356-0.4 wt% Sc alloys in the T6 condition. Pramod et al. [31] also reported improvements in tensile strength with Sc additions of 0.4 wt% in both as-cast and T6 conditions. The YS increased to 123 MPa for as-cast and 245 MPa for T6 condition. Whereas the UTS improved to 216 MPa in as-cast and 300 MPa in T6 condition. The ductility increased to 8% for as-cast and 8.4% for T6 condition. On the other hand, Lim et al. [32] reported a higher strength of 338 MPa for alloys containing 0.6 wt % Sc; however, according to this study, higher Sc levels would deteriorate the mechanical properties. Similarly, Lu and Zhang [33] obtained higher mechanical properties in as-cast conditions compared to our study. According to them, adding 0.54 wt% Sc resulted in YS of 153.2 MPa, UTS of 239.1 MPa and elongation of 5.3%.

4. Discussion

4.1. *Effect of Sc on solidification path and nucleation behaviour*

The combined Scheil-Gulliver simulations and DSC thermal analysis provide insights into the solidification behaviour of A356.2 and Sc-modified alloys. Both approaches reveal that Sc significantly in-

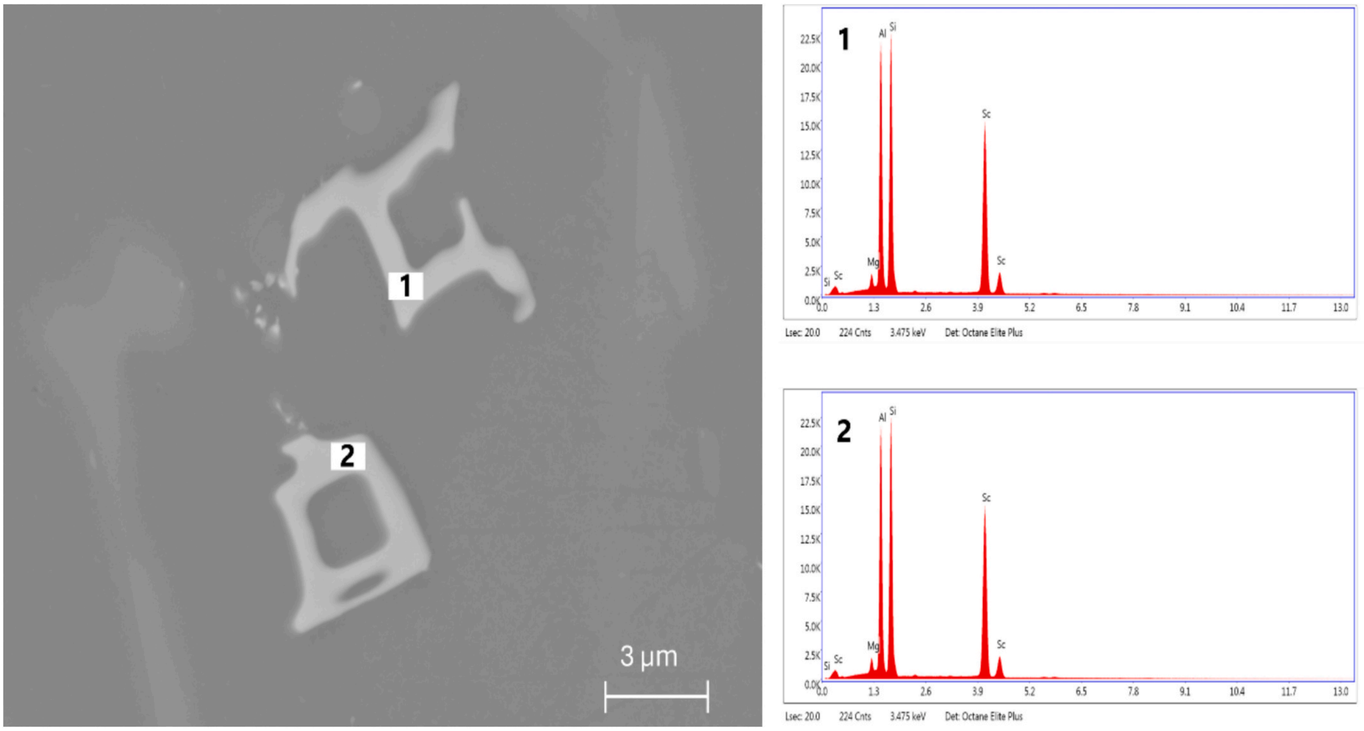

Fig. 10. Hollow frame-like $AlSc_2Si_2$ morphology in A356-0.2Sc alloy along with their EDS spectra.

fluences the sequence and thermodynamics of phase formation during solidification, although the overall freezing range remains largely unchanged. In the baseline A356.2 alloy, the solidification path follows the conventional sequence:

$$L \rightarrow \alpha\text{-}Al;\ L \rightarrow \alpha\text{-}Al + Si;\ \ L \rightarrow \alpha\text{-}Al + Si + Mg_2Si,$$

The nucleation of primary α-Al begins at approximately 615.2 °C, followed by the eutectic reaction near 574.8 °C, and solidification completes around 558.7 °C. These results correspond closely with DSC data, which indicate a liquidus at 616.7 °C and a solidus at 558.8 °C. The microstructure is thus dominated by α-Al (over 90%), with Si and Mg_2Si forming the characteristic interdendritic eutectic structure.

With Sc addition, the solidification path becomes distinctly modified, even though the liquidus remains nearly constant (615 °C). At 0.2 wt% Sc, a new ternary intermetallic phase, $AlSc_2Si_2$, appears near 570 °C and coexists with α-Al and Si during the final stages of solidification. The formation of this phase slightly reduces the Si content in the remaining liquid (0.8% reduction compared to the baseline alloy), limiting the growth of coarse eutectic Si. This minor consumption of Si (0.2% phase fraction) is beneficial for eutectic refinement while still preserving sufficient Si and Mg for Mg_2Si precipitation during ageing. As the Sc content increases to 0.4 wt%, $AlSc_2Si_2$ forms slightly earlier (571.7 °C) and its fraction increases (0.6%). The DSC thermograms show a slight depression in the eutectic peak temperature to 571.9 °C and 571.1 °C for the 0.2 wt% and 0.4 wt% Sc alloys, respectively. This shows that the thermodynamic stability of the $AlSc_2Si_2$ intermetallic increased and demonstrated stronger interaction between Sc and Si. The persistence of $AlSc_2Si_2$ through the later stages of solidification helps to produce a uniform distribution of Sc-rich intermetallics in the α-Al matrix with a refined microstructure. The suppression of the equilibrium amount of residual Si in the liquid (6.3%) at this composition is consistent with the observed transformation in the eutectic Si to a finer, fibrous morphology. At 0.6 wt% Sc, the solidification path changes substantially. The $AlSc_2Si_2$ phase forms as early as 582.1 °C, prior to Si precipitation and continues to grow throughout solidification, reaching a fraction of 0.9%. This early formation consumes Si from the liquid before eutectic nucleation, alters the chemistry of the residual melt and promotes the growth of coarser, blocky $AlSc_2Si_2$ morphologies in the α-Al matrix. This is supported by the DSC results, which show a small increase in the liquidus, eutectic, and solidus temperatures to 618.6 °C, 572.2 °C, and 557.1 °C, respectively. This indicates that high amounts of Sc addition suppress the eutectic modification effect, leading to reduced undercooling and a partial reversion toward coarser, less fibrous Si morphology in the 0.6 wt% Sc alloy.

4.2. Grain Refinement, modification of eutectic Si and Fe-bearing intermetallics

The optical micrographs and polarized light images of the anodized samples (Fig. 5) confirm that Sc additions result in significant refinement of the α-Al grains along with a reduction in the SDAS. The baseline A356.2 alloy has coarse, columnar dendritic α-Al grains of size 540 ± 39 µm with an SDAS of 24 µm. The grain size of the alloy reduces to 338 ± 26 µm when 0.2 wt% Sc is added and to a minimum of 260 ± 22 µm when 0.4 wt% Sc is added, with the SDAS reducing to a minimum of 19.7 µm. Also, as can be seen from Fig. 5, the eutectic Si morphology modifies with Sc addition. The baseline A356.2 alloy shows a network of acicular, plate-like Si particles. In contrast, alloys with Sc exhibit fragmented, fibrous, and more rounded Si morphologies distributed along interdendritic boundaries. This refinement can be attributed to the combined effects of solute-induced constitutional undercooling and enhanced heterogeneous nucleation associated with Sc-containing phases.

During the early stages of solidification, Sc exhibits a strong tendency to segregate into the liquid phase due to its low equilibrium partition coefficient ($k < 1$) and steep liquidus slope (m). This segregation establishes a solute boundary layer ahead of the solid–liquid interface, creating constitutional undercooling that restricts the growth of existing α-Al dendrites. The degree of growth restriction can be described using the growth restriction factor (Q), given by $Q = m(k - 1)C_0$ (1).

where m is the slope of the liquidus line, k the solute partition coefficient, and C_0 the initial solute concentration. In multicomponent systems such as A356-Sc, the total Q can be approximated by summing

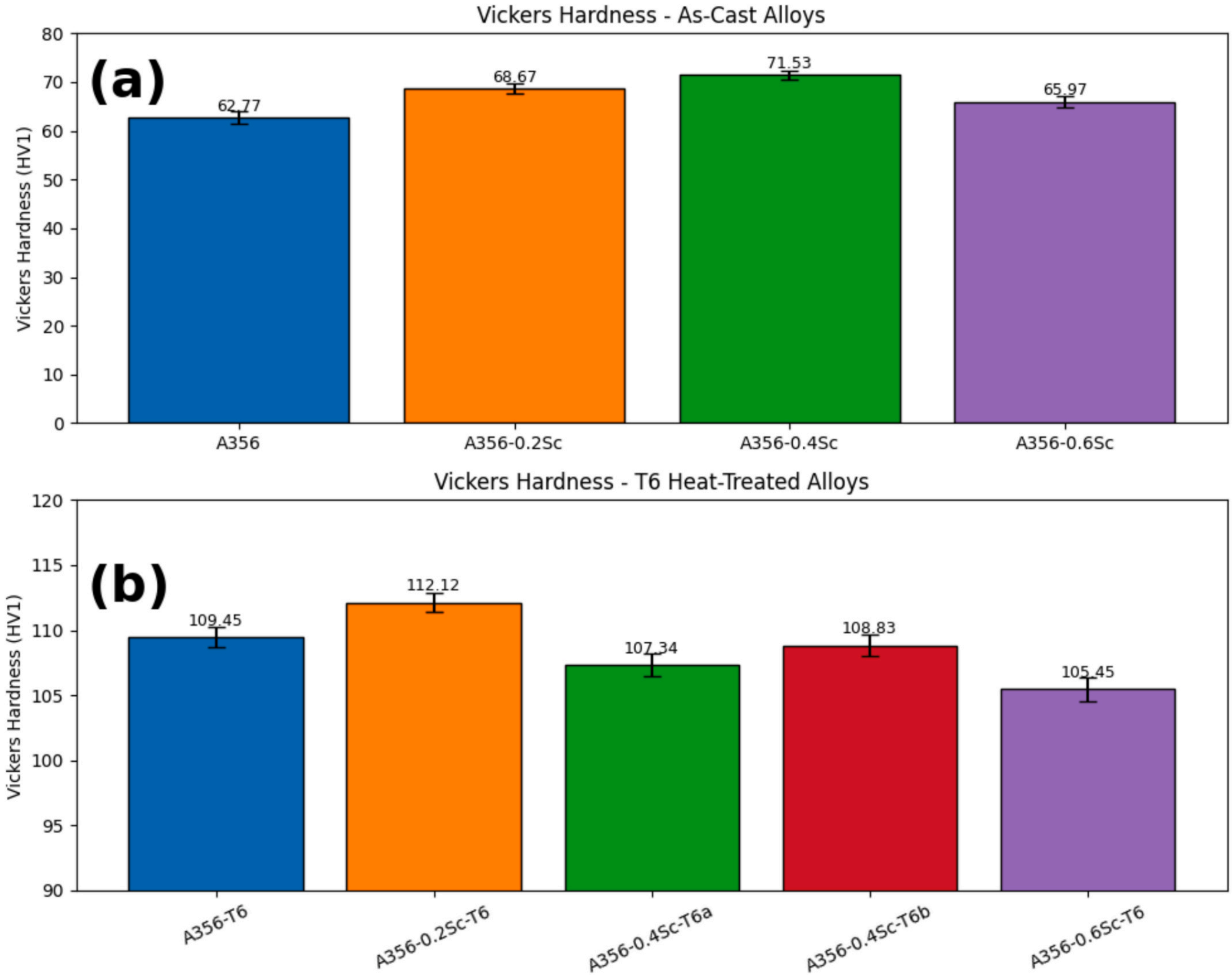

Fig. 11. Vickers hardness of A356 alloys with varying Sc content in (a) as-cast and (b) T6 heat-treated conditions.

the contribution of each solute (ex: Si, Ti, Sc) when the alloy is dilute. Sc contributes a particularly large Q value because it has one of the smallest k values. As a result, Sc additions substantially increase Q, leading to a lower dendrite growth rate and finer α-Al grains. Physically, this means that Sc accumulation ahead of the dendrite tip induces a compositional gradient and localised undercooling, which retards dendrite coarsening and promotes the formation of new nuclei. This mechanism effectively explains the observed reduction in both grain size and SDAS in the Sc-modified alloys. However, according to Pandee et al. [34], Sc additions do not increase the growth restriction factor significantly, hence the solute effect alone cannot be the primary grain refining mechanism in this alloy system.

The grain refinement of these alloys is further supported by thermal analysis. Cooling-curve measurements as shown in Fig. 15(a) reveal that the α-Al nucleation temperature increases slightly from 615.2 °C in the baseline alloy to 617.3 °C in A356-0.4Sc, while the undercooling and recalescence decrease notably as shown in

Table 5. This behaviour indicates that Sc enhances nucleation efficiency by providing potent heterogeneous nucleation sites and increasing constitutional undercooling. The reduced recalescence peak suggests that numerous nuclei form almost simultaneously leading to a refined grain structure. Most studies on Al-Si cast alloys with Sc addition also highlight the formation of coherent Al_3Sc particles which act as the nucleation sites for the α-Al formation [31,35–39]. These particles exhibit a very low lattice misfit of 1.5% with α-Al, providing favourable heterogeneous nucleation sites.

Although Al_3Sc is widely recognised as a potent heterogeneous nucleation site in wrought Al-Sc alloys due to its coherent $L1_2$ structure and very low lattice mismatch with α-Al (<1.5%), no stoichiometric Al_3Sc precipitates were detected in the present A356-Sc cast alloys. Instead, under the Si-rich solidification conditions of A356 alloy, Sc preferentially forms Si-containing intermetallic compounds. Fig. 13 presents low-magnification and atomic resolution high angle annular dark field – scanning transmission electron microscopy (HAADF-STEM) images, together with the corresponding elemental maps, of the A356-0.4Sc alloy. STEM-EDS mapping demonstrates strong co-localisation of Sc and Si within these particles, with minor Ti enrichment. Quantitative EDS analysis of the Sc-rich phase shows: Al 62.63 at. %, Si: 15.77 at. %, Sc: 20.42 at. % and Ti: 1.18 at. %. This composition clearly deviates from Al_3Sc and instead corresponds closely to an $(Al,Si)_3(Sc,Ti)$ formulation.

High-resolution HAADF – STEM imaging combined with Fast Fourier Transform (FFT) analysis indexed along the [110] zone axis reveals a cubic structure consistent with the $L1_2$-type lattice (space group Pm3¯m). The FFT pattern shows characteristic {1 1 0} and {1 1 1} reflections of a face-centred cubic lattice, together with weak {0 0 1} superlattice reflections confirming the presence of an ordered $L1_2$ structure. Moreover, the presence of well-defined spots without streaking or splitting indicates a coherent or near-coherent relationship with

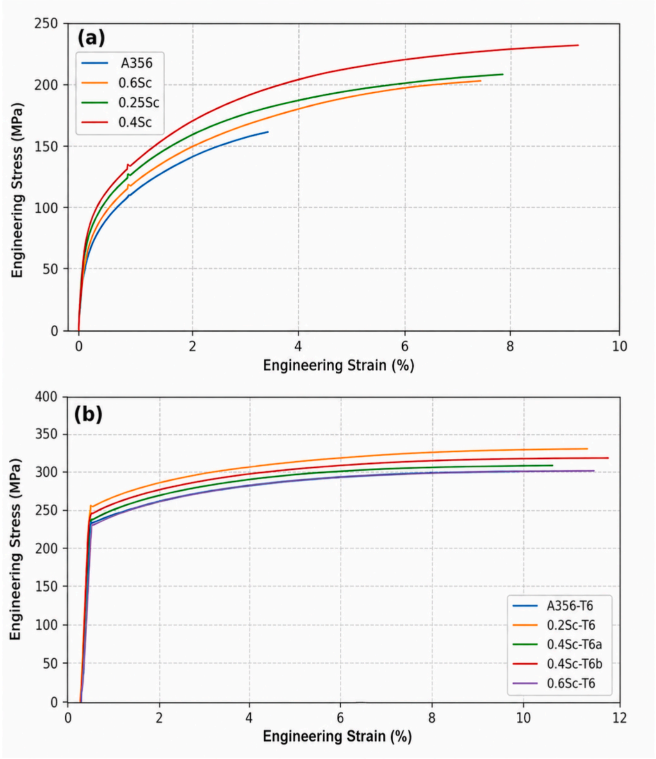

Fig. 12. Representative engineering stress–strain curves of A356 alloys with varying Sc content in (a) as-cast and (b) T6 conditions.

the α-Al matrix. This coherency strongly supports the conclusion that the observed nanoscale particles are not the tetragonal V-phase ($AlSc_2Si_2$), but rather a cubic $(Al,Si)_3(Sc,Ti)$ phase derived from the Al_3Sc structure through Si and Ti substitution. This is consistent with the similarity of the atomic radii of Si and Al [40], and with the partial substitution of Ti for Sc at low concentrations. Mao et al. [41] observed similar phase in an Al-7Si-0.6 Mg alloy and suggested that this phase could be responsible for the grain refinement in high Si cast alloys. Similarly, in the Al-Si-Zr-Ti systems, Sanchez et al. [42] found that the $(Al,Si)_3(Zr,Ti)$ phase acted as nucleation sites for the Al phase to grow instead of Al_3Zr or Al_3Ti.

The absence of discrete Al_3Sc precipitates suggests that any transient Al_3Sc formed during early solidification is unstable in the presence of Si and undergoes transformation to the more stable Al-Si-Sc during solidification or subsequent solution treatment. This transformation is driven by the strong chemical affinity between Sc and Si and is consistent with the thermodynamic assessments of the Al-Si-Sc system, which predict $AlSi_2Sc_2$ phase to be thermodynamically favoured over Al_3Sc under Si-rich conditions due to a more negative formation enthalpy of the former [43]. Fig. 14 presents STEM images of the tetragonal $AlSi_2(Sc, Ti)_2$ phase in the as-cast A356-0.4Sc alloy together with the corresponding EDS maps, the FFT pattern indexed along the [130] zone axis and a simulated diffraction pattern of the $AlSi_2Sc_2$ phase. Wang et al. [44] also reported that in Al-Si-Sc alloys, Al_3Sc and $AlSi_2Sc_2$ compete for Sc solute. The initially formed Al_3Sc nuclei may have the possibility of peritectic transformation with the Si-rich liquid via: $L + Al_3Sc \rightarrow AlSi_2Sc_2$ at 625 °C, or through a subsequent eutectic transformation: $L \rightarrow Al + Si + AlSi_2Sc_2$ at 573 °C. As the solidification progresses, the initially formed Al_3Sc nuclei will be consumed through the above transformation, leading to a microstructure consisting of $AlSi_2Sc_2$ at α-Al interfaces. This mechanism explains both the enhanced nucleation efficiency (due to transient Al_3Sc) and its apparent disappearance in the as-cast structure. Also, this $AlSi_2(Sc, Ti)_2$ phase is a variant of the $AlSi_2Sc_2$ phase, where Ti partially substitutes Sc in the lattice and hence the overall crystal structure remains the same. Further, Xiang et al. [45] demonstrates the precipitation mechanism of this phase as follows: as-cast state → Si-dispersoids → Si, Sc, Zr, Ti-rich Al matrix → $AlSi_2(Sc, Ti)_2$ precipitates precipitating during solution treatment. A similar precipitation mechanism is described by Dumbre et al. [46] for the precipitation of $AlSi_2Sc_2$ phase from $(Al, Si)_3Sc$ nano-precipitates.

Hence, the grain refinement in Sc-modified alloys is primarily attributed to the formation of Sc-containing particles such as $(Al,Si)_3(Sc, Ti)$, which could act as effective heterogeneous nucleation sites for primary α-Al, along with the contribution of solute Sc to constitutional undercooling that restricts dendrite growth.

Apart from the refinement in the grain size with Sc addition, the eutectic morphology also undergoes a significant transformation from plate-like to a more fibrous and fragmented morphologies as can be seen from Fig. 15. Identifying the exact modification mechanism is beyond the scope of this study, however, many studies [34,37,47–50] have considered these mechanisms and these have been referred to in brief in this study.

During the eutectic stage, the cooling curve as shown in Fig. 15(b) display pronounced changes in both the eutectic growth temperature and recalescence with increasing Sc content. Compared to the baseline A356 alloy, the Sc-containing alloys exhibit noticeable changes in the cooling behaviour, particularly in the eutectic region. The unmodified A356.2 exhibits minimal recalescence of 0.7 K, while A356-0.2Sc and A356-0.4Sc show increasing values of approximately 3.8 K and 4.4 K, respectively, while 0.6Sc alloys show a marginal decrease in the recalescence value to 2.8 K, which is still higher than the baseline alloy. Similarly, the eutectic growth temperature of A356.2 alloy decreased from 573.3 °C to 566.7 °C with 0.4 Sc addition. The decrease in the eutectic growth temperature and the enhanced recalescence indicates eutectic modification [51]. Prukkanon et al. [47] also observed the similar behaviour in the cooling curves of Sc added A356 alloys. They proposed that the extra undercooling and recalescence that occurs is due to the energy required to absorb Sc at the interface advancing Si phase and that the intermetallic phase contains Al-Sc-Si, poisoning the twin-plane re-entrant (TPRE) growth mechanism. This transformation can be explained as follows: during solidification, Sc reacts with Si to form $AlSc_2Si_2$, which locally depletes Si concentration and alters the chemical potential of the remaining liquid. This reduces the supersaturation driving force for faceted Si growth, resulting in fine fibrous morphologies. Also, the surface tension of aluminium decreases with Sc addition and hence, the surface energy of Al/Si interface also changes, affecting both the nucleation and growth of Si in the eutectic reaction. However, some studies revealed high twinning density in the Sc modified eutectic Si corresponding to the impurity-induced twinning (IIT) mechanism [48,49]. According to this, Sc atoms are adsorbed onto the growth

Table 5
Temperatures recorded in the cooling curves of A356.2 and Sc-modified A356 alloys.

Alloy	Liquidus (°C)	Nucleation (°C)	Recalescence Undercooling (ΔT, K)	Theoretical Eutectic (°C)	Eutectic Temp (°C)	Eutectic Depression (K)	Eutectic Recalescence (K)
A356.2 (Baseline)	619.5	615.2	1.8	573.6	573.3	0.3	0.7
A356-0.2Sc	618.9	615.3	1.0	572.8	566.6	6.2	3.8
A356-0.4Sc	620.3	617.3	0.5	573.1	566.7	6.4	4.4
A356-0.6Sc	620.6	617.6	0.4	573.1	567.9	5.2	2.8

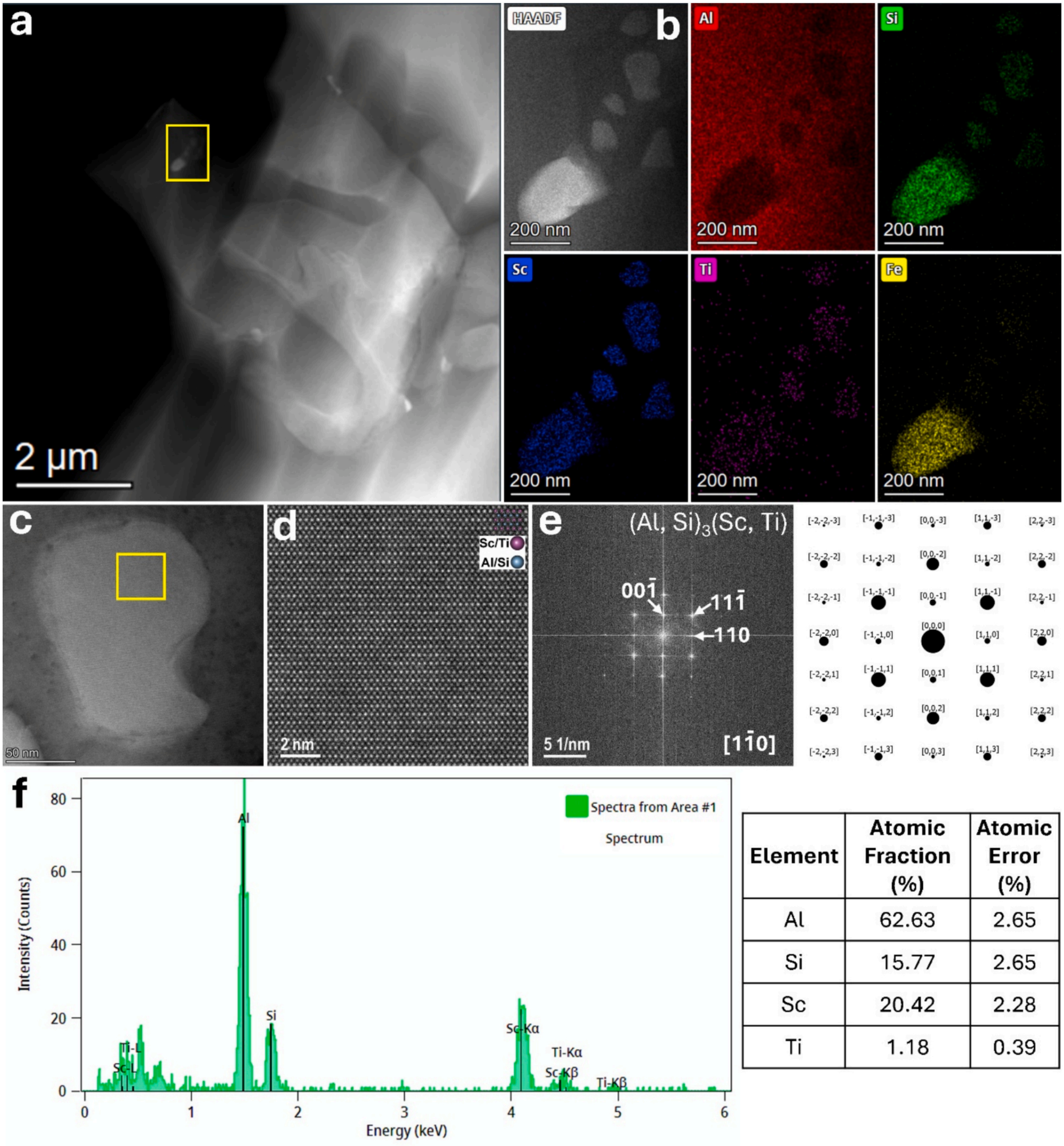

Element	Atomic Fraction (%)	Atomic Error (%)
Al	62.63	2.65
Si	15.77	2.65
Sc	20.42	2.28
Ti	1.18	0.39

Fig. 13. STEM characterisation of the (Al,Si)$_3$(Sc,Ti) phase in A356-0.4Sc alloy: (a) Low-magnification HAADF – STEM image of the A356-0.4Sc alloy; (b) HAADF – STEM image showing coarse Sc-rich particles within the α-Al matrix, together with corresponding STEM-EDS elemental maps (Al, Si, Sc, Ti, Fe) revealing pronounced co-enrichment of Sc and Si, minor Ti substitution and negligible Mg incorporation; (c) HAADF-S TEM image of an individual (Al,Si)$_3$(Sc,Ti) particle; (d) Atomic-resolution HAADF-STEM image enlarged from the yellow-marked region in (c), revealing an ordered atomic arrangement, characteristic of Al$_3$Sc structure; (e) FFT pattern indexed along the [110] zone axis, showing reflections consistent with a cubic L1$_2$-type (Al,Si)$_3$(Sc,Ti) structure. The simulated diffraction pattern of Al$_3$Sc is shown for comparison; and (f) EDS spectrum extracted from the individual particle in (c), along with its quantification, showing dominant Al, Si and Sc peaks with minor Ti.

planes of Si, promoting twin formation during growth. Each twin acts as a nucleation site for subsequent branching, converting faceted Si into a fibrous network. Wang et al. [50] used HAADF-STEM imaging studies, showcasing that Sc modifies eutectic Si through a combined IIT-TPRE mechanism, by Al-Si-Sc nanoclusters. In the IIT mechanism, these clusters stimulate frequent twin formation within growing Si. Sc addition produces dense micro-twins at 70.5° and stacking faults on {111} planes, generated by the localised lattice distortion caused by these Al-

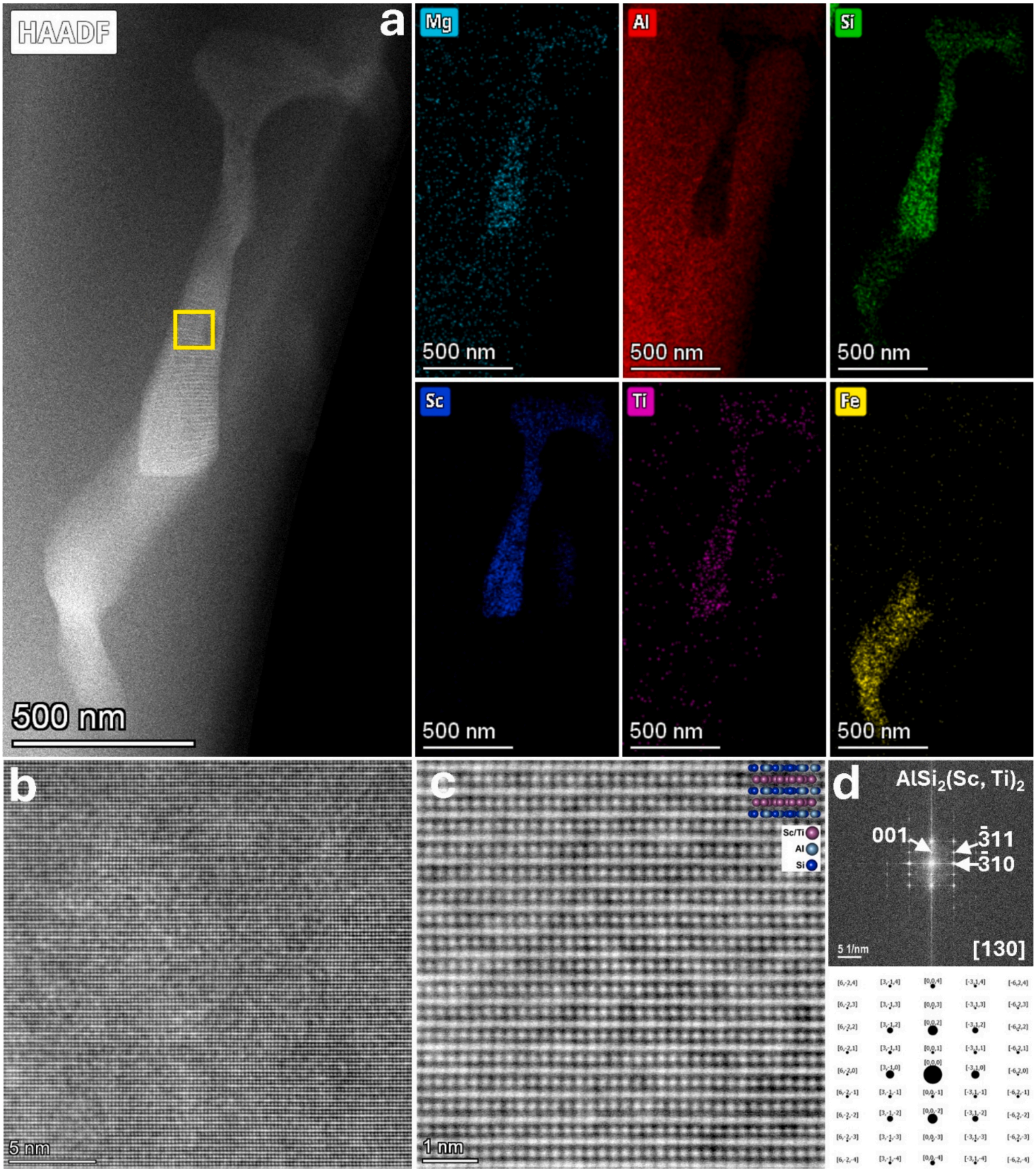

Fig. 14. STEM characterisation of the $AlSi_2Sc_2$ phase in A356-0.4Sc alloy: (a) HAADF-STEM image and corresponding STEM-EDS maps showing co-enrichment of Sc and Si; (b), (c) atomic-resolution HAADF-STEM images; and(d) FFT pattern corresponding to (b), indexed along the [130] zone axis, confirming the tetragonal $AlSi_2Sc_2$ structure.

Si-Sc clusters. These twins promote branching and refine the Si network. Simultaneously, the TPRE poisoning mechanism becomes active as Sc atoms and Al-Si-Sc clusters preferentially adsorb at re-entrant edges along $< 112 >$ growth directions, hindering Si attachment and suppressing faceted plate growth. This interference forces Si to grow laterally, increasing twin density, resulting in fibrous morphologies. Wang et al. [50] also demonstrated that the modified eutectic Si exhibited dendritic growth, forming several twin branches at 35.25° and 54.75° angles. Apart from the formation of numerous twins, Sc additions led to the formation of stacking faults and Al-Sc-Si nanoclusters, which segregated at the 70.5° twin intersections and twin fronts of the Si phase and also aligned linearly along the $< 112 >$ growth direction of Si. So, unlike the conventional IIT and TPRE poisoning mechanism, the segregation of Al-Sc-Si nanoclusters within the eutectic Si led to the formation of micro-twins or stacking faults. Additionally, it is known that Phosphorous (P), present in trace amount in Al-Si alloys, acts as a potent nucleation site for eutectic Si through the formation of AlP particles [10]. According to Pandee et al. [34,37], when Sc is added to these alloys, instead of AlP, ScP is formed, which settles under gravity either prior to the Al nucleation or during the early stage of primary Al solidification, thus reducing the nucleation frequency of Sc and the growth of a Si-containing eutectic front.

Hence, the modification of eutectic Si is associated with the interaction of Sc with the solidification front, where Sc and Al-Si-Sc clusters

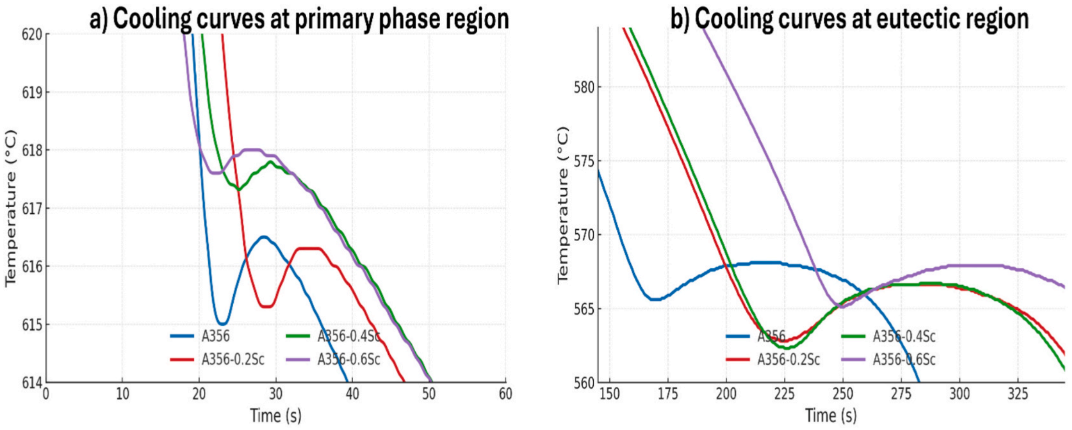

Fig. 15. Experimentally obtained cooling curves of A356.2 and Sc-modified A356 alloys showing (a) primary α-Al nucleation region and (b) Al-Si eutectic reaction region.

influence Si growth through combined impurity-induced twinning (IIT) and twin-plane re-entrant edge (TPRE) poisoning mechanisms, resulting in a transition from coarse plate-like to fine fibrous morphology.

Apart from the grain refinement and modification in the morphology of eutectic Si, another minor yet very important aspect of adding Sc in Al alloys is the change in the chemistry and the morphology of Fe-bearing intermetallics. It is known that Fe-rich intermetallics, especially the β-Al_5FeSi phase, are among the most detrimental phases in Al-Si cast alloys due to their platelet morphology, which acts as stress concentrator leading to crack initiation. In the baseline A356.2 alloy, β-Al_5FeSi forms late in solidification within interdendritic regions. With Sc addition, both the morphology and chemistry of Fe phases are substantially modified as shown in Fig. 8 and Fig. 9. Fig. 13, Fig. 14 and Fig. 16 also depicts the modified morphology of the Fe-bearing intermetallic compound. Interestingly, from all the images it can be seen that it is precipitated along with the Sc-bearing compounds. The β-Al_5FeSi platelets are replaced by compact, Chinese-script or nodular Al-Fe-Si-Sc and Al-Fe-Si-Sc-Mg based intermetallics. Tzeng et al. [52] identified the Sc-Fe-Mg-based phase as $Al_{12}Si_6Fe_2(Mg, Sc)_5$ which has a lower hardness and elastic modulus than the β-Al_5FeSi phase and hence is therefore less likely to initiate cracks. Tzeng et al. [52] also suggested that this nodular phase can improve the fluidity of the alloy, reducing interdendritic shrinkage. Pramod et al. [31] identified the phases to be $Al_5Fe(Si, Sc)$ and $Al_8Mg_3Fe_1(Si, Sc)_6$ and claimed that these phases are less

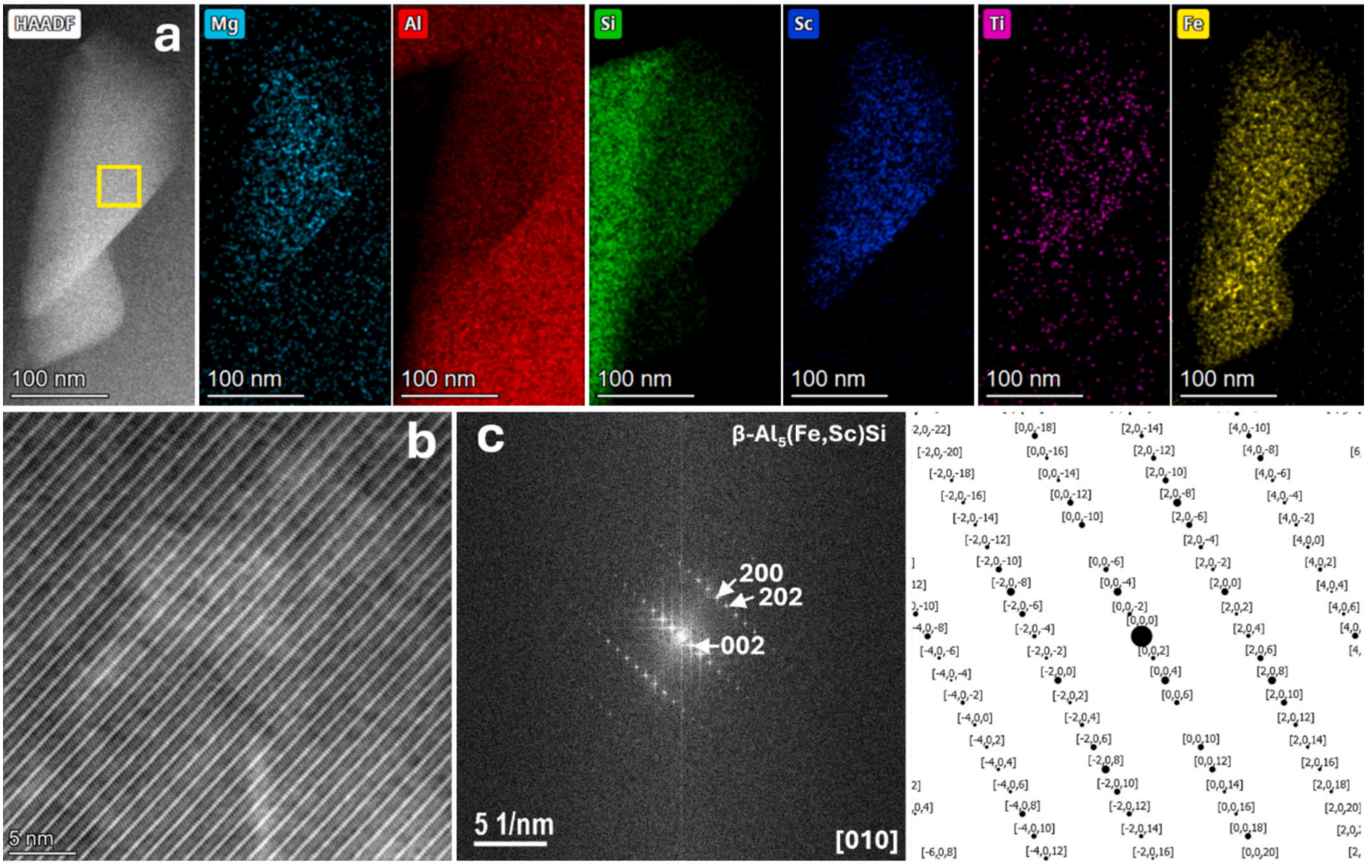

Fig. 16. STEM characterisation of the Fe-based intermetallic with: (a) HAADF-STEM image of the Sc-modified β phase with the corresponding EDS elemental maps; (b) atomic-resolution HAADF-STEM image of the β phase; and (c) FFT pattern generated from (b) together with the simulated diffraction pattern of the β phase.

detrimental to the mechanical properties of the alloy, especially the ductility. The chemical compositions of these intermetallics as shown in Table 4 shows that the chemistry of these phases matches with those reported by Pramod et al.[31]. They explained that this transformation in the morphology of Fe-rich intermetallics is driven by the excess Sc available in the interdendritic liquid, which diffuses to the secondary phases like Al_5FeSi, $AlSc_2Si_2$ and $Al_8Mg_3Si_6Fe$ and substitutes for Si in these intermetallics. This is the reason why the fish-bone shaped Fe-rich intermetallic precipitated on the $AlSc_2Si_2$ phase as shown in Fig. 9. Similar observations were made by Zhang et al. [53].

4.3. Strengthening mechanisms in as-cast alloys and Correlation with mechanical properties

The significant improvement in the strength and ductility of the as-cast A356-0.2Sc and A356-0.4Sc alloys can be explained by a combination of grain-boundary strengthening, the refinement of the dendritic structure, modification of the eutectic, the transformation of Fe-intermetallics, and the strengthening caused by Sc-containing dispersions.

The pronounced refinement of the primary α-Al grains (52% reduction at 0.4 wt% Sc) and the reduction in the SDAS (19% reduction at 0.4 wt% Sc) provide a substantial contribution through grain-boundary strengthening, as described by the Hall-Petch relationship: $\sigma_y = \sigma_0 + kd^{-1/2}$, where the increased grain-boundary density effectively impedes dislocation motion [54,55]. Furthermore, SDAS refinement reduces solute microsegregation and local stress concentrations, promoting more homogeneous plastic deformation. The refined grain structure and dendritic network can also influence melt feeding during solidification. The transition from coarse dendritic to fine equiaxed grains is expected to enhance interdendritic feeding pathways, which may reduce the likelihood of shrinkage porosity formation, thereby improving cast integrity and delaying strain localisation during tensile loading [56]. At the same time, Sc addition transforms eutectic Si from coarse, plate-like morphologies to fine fibrous or fragmented network, thereby reducing stress concentration at the Si/matrix interface, suppressing early crack initiation and absorbing more plastic strain, leading to improved elongation and fracture resistance. The refined eutectic network additionally enhances load transfer between α-Al and Si, contributing indirectly to strength. This effect is further reinforced by the suppression and morphological transformation of the Fe-bearing intermetallics, where the brittle β-Al_5FeSi plates are replaced by compact, nodular Al-Fe-Si-Sc and Al-Fe-Mg-Si-Sc phases with lower elastic modulus and reduced crack-initiating tendency, contributing primarily to ductility improvement while maintaining the strength.

These finely dispersed Sc-containing particles contribute significantly to strengthening via the Orowan bypass mechanism, whereby closely spaced, hard dispersoids impede dislocation motion, leading to an increase in yield strength proportional to particle density and inversely proportional to interparticle spacing [77]. Their uniform distribution also promotes dislocation accumulation and local pinning, enhancing work-hardening capacity. Solid-solution strengthening from Sc is expected to be limited due to its low equilibrium solubility in Al [78]; however, a slight increase in the Al lattice parameter reported in Sc-containing alloys may provide a minor additional contribution [39].

In addition to these microstructural refinements, dispersion strengthening from Sc-containing nanoscale particles plays a crucial role. Fig. 13 shows the STEM images of the as-cast A356-0.4Sc alloy, revealing the presence of Sc-rich phases within the α-Al matrix. The presence of these dispersoids explains the weak but distinct extra reflections observed in FFT patterns as shown in Fig. 13 and Fig. 14, confirming the presence of ordered second phases formed during solidification. Fig. 17 reveals dense nanoscale features attributed to Sc-rich clusters. These clusters contribute to strengthening via

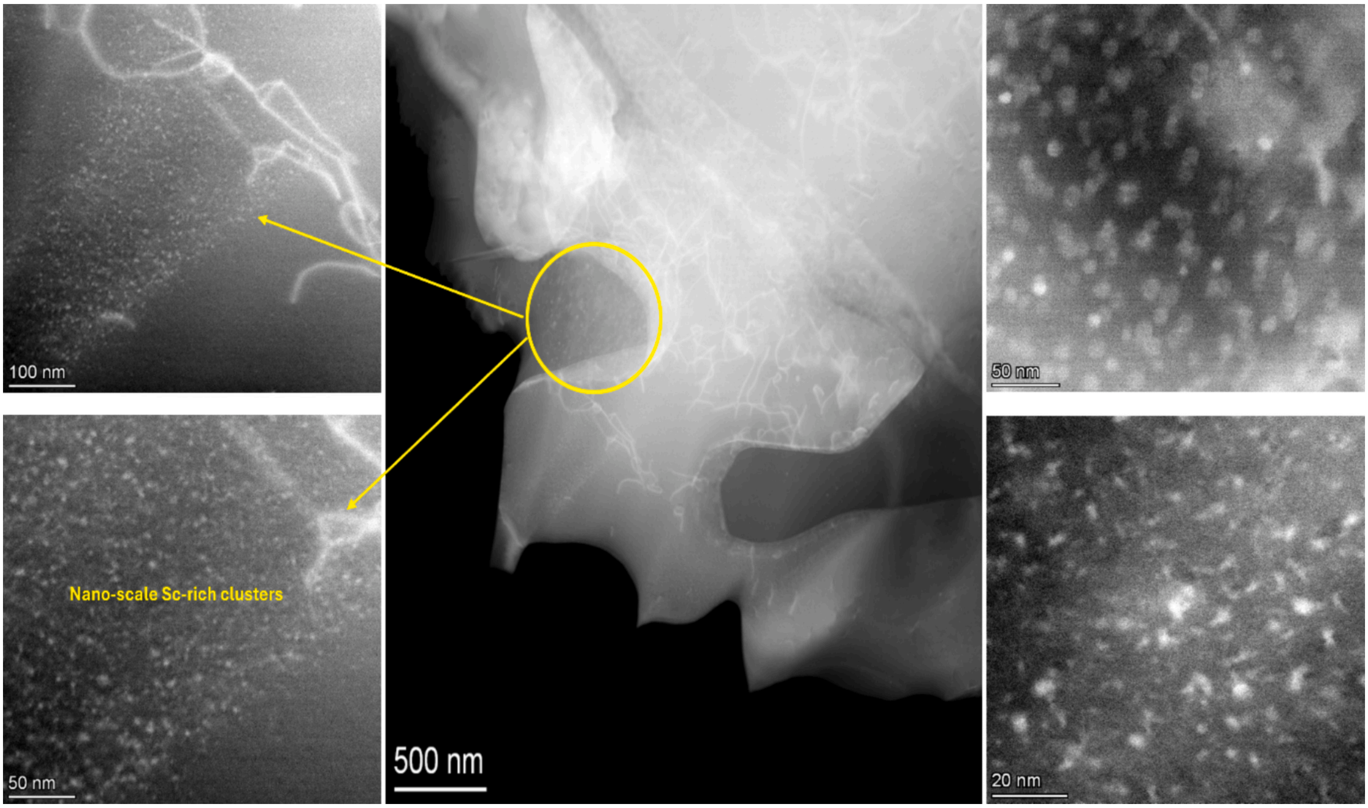

Fig. 17. STEM overview image showing a region of the as-cast A356-0.4Sc alloy. The central low-magnification image highlights the analysed area (yellow circle), with higher-magnification HAADF-STEM images revealing clusters of Sc-rich features within the α-Al matrix. The features appear locally aggregated rather than uniformly dispersed.

dislocation–cluster interactions, increasing resistance to plastic deformation and enhancing yield strength and work hardening [79].

According to some studies the solid solution strengthening from Sc in Al should be very low due to its limited solubility in Al [57], however, according to other studies the lattice parameter of Al increases slightly with Sc addition, which might contribute to solid solution strengthening [31]. These mechanisms act simultaneously, thereby enhancing both strength and ductility with the addition of Sc, which explains why A356-0.4Sc exhibits optimal mechanical characteristics and hardness in the as-cast condition. The combined strengthening response can therefore be expressed as:

$$\Delta\sigma_{\text{total}} = \Delta\sigma_{\text{GB}} + \Delta\sigma_{\text{SS}} + \Delta\sigma_{\text{disp}} + \Delta\sigma_{\text{MS}} \tag{2}$$

where the individual terms represent contributions from grain-boundary strengthening, solid-solution strengthening, dispersion strengthening by Sc-containing dispersoids and microstructural strengthening arising from eutectic refinement, SDAS reduction, and Fe-intermetallic modification. Among the compositions investigated, A356-0.4Sc shows the most favourable balance of these mechanisms, resulting in optimal mechanical performance in the as-cast condition.

4.4. *Optimum Sc addition range in A356 alloy*

The combined analysis of thermodynamic predictions, solidification behaviour, microstructural evolution, and mechanical properties clearly indicates that the beneficial effects of Sc addition in A356 alloy are strongly dependent on and governed by the stability and formation sequence of Sc-containing intermetallic phases during solidification. Hence, there is a narrow optimum Sc addition range in A356 alloys. Within this range, Sc effectively enhances grain refinement, eutectic modification, and dispersion strengthening without adversely altering the solidification path or heat-treatment response.

For Sc additions up to 0.4 wt%, the solidification sequence remains dominated by primary α-Al formation followed by the Al-Si eutectic reaction, with $AlSc_2Si_2$ forming only during the final stages of solidification near the conventional eutectic temperatures. As shown by the Scheil calculations in Fig. 2b and d, $AlSc_2Si_2$ appears at 570–572 °C for 0.2–0.4 wt% Sc, after α-Al nucleation and along with eutectic solidification. In this composition range, the volume fraction of $AlSc_2Si_2$ remains limited (<0.6%) as shown in Fig. 3, and its formation is sufficiently delayed such that it does not interfere with primary α-Al growth.

This delayed formation of $AlSc_2Si_2$ is critical. It allows Sc to act initially as an effective grain refiner through transient solute segregation and heterogeneous nucleation effects, while also promoting eutectic Si modification and refinement of Fe-bearing intermetallics. Experimentally, this is reflected in the substantial reduction in grain size, SDAS, and the transformation of eutectic Si from coarse plates to a fine fibrous morphology. As a result, the A356-0.2Sc and A356-0.4Sc alloys exhibit a unique combination of increased YS, YTS and elongation, a rare but highly beneficial property for cast Al-Si-Mg alloys.

In contrast, when the Sc content exceeds about 0.52 wt%, not only do the experimental and thermodynamic predictions indicate a fundamental change in the solidification behaviour, but also, as shown in the equilibrium phase diagram in Fig. 18, $AlSc_2Si_2$ begins to form at significantly higher temperatures and enters the primary solidification regime, co-precipitating from the melt together with α-Al. This behaviour is evident in the A356-0.6Sc alloy investigated in this study, where $AlSc_2Si_2$ starts to form at 582 °C through an early $L \rightarrow \alpha\text{-Al} + AlSc_2Si_2$ reaction well before the Al-Si eutectic reaction as shown in Fig. 2d and Table 2. Furthermore, coarse, elongated and blocky $AlSc_2Si_2$ intermetallic compounds are observed within the α-Al matrix, with measured lengths of approximately 30–32 μm (see Supplementary Fig. 1). The microstructural details are shown in Fig. 19.

The early formation and significant growth of primary $AlSc_2Si_2$ have

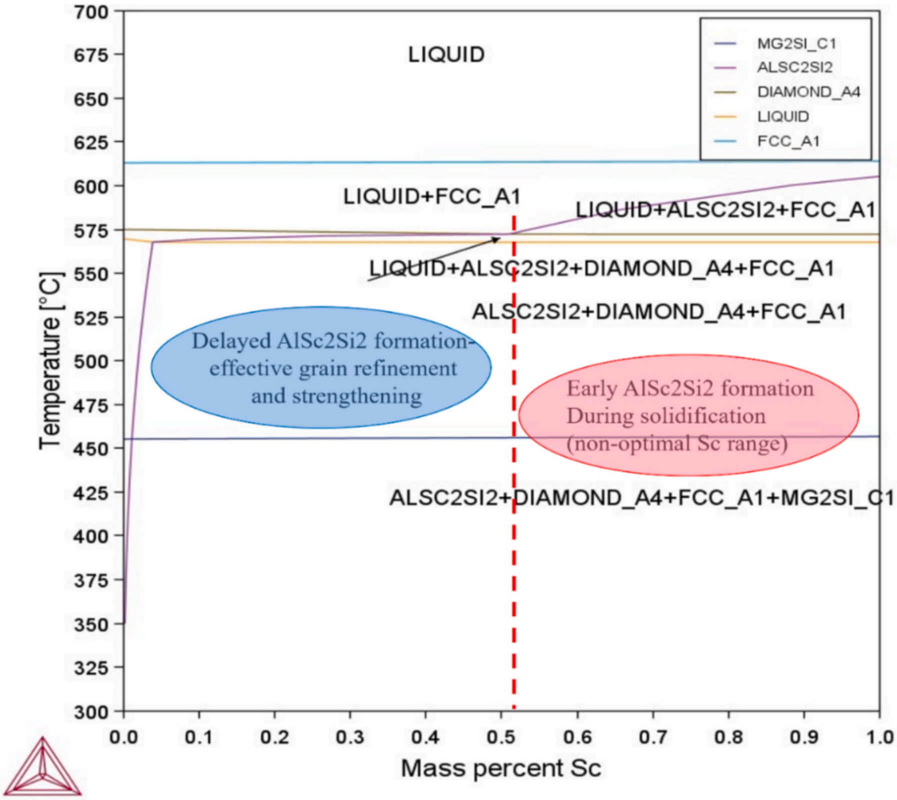

Fig. 18. Equilibrium phase diagram of A356-Sc system showing the evolution of phase stability with increasing Sc content, depicting the onset of primary $AlSc_2Si_2$ formation above 0.52 wt% Sc.

several detrimental effects as observed in the alloy with 0.6 wt% Sc. First, it consumes a significant fraction of available Sc and Si during the early stages of solidification, reducing the solute content of the remaining liquid and weakening constitutional undercooling effects which can be observed in terms of a slight increase in the grain size and SDAS of these alloys and also the effect on eutectic Si modification diminishes. This is visible from the lowering of eutectic recalescence as presented in Table 5. Second, because of the coarse morphology, $AlSc_2Si_2$ act as a local stress concentrator rather than effective strengthening dispersoids.

The mechanical property trends are co-related with the microstructural transition. While the yield strength and ductility increase significantly from the baseline alloy to 0.4 wt% Sc due to the strengthening mechanisms explained in the previous section, further Sc addition leads to a decline in strength and a slight loss of elongation. Sc additions beyond 0.52 wt% should therefore be avoided, as they promote primary $AlSc_2Si_2$ formation during solidification, leading to microstructural coarsening and deterioration in mechanical properties. Therefore, a clear optimal Sc addition range between 0.2 and 0.4 wt% for A356 alloys is established by the combined evidence from phase-diagram analysis, cooling-curve measurements, microstructural characterisation and mechanical testing.

Apart from these microstructural and thermodynamic considerations, the practical applicability of Sc additions must also be evaluated. Although Sc is a relatively expensive alloying element, the present study demonstrates that only a limited addition (0.2–0.4 wt%) is required to achieve significant simultaneous improvements in strength and ductility. This optimised addition range ensures efficient utilisation of Sc, avoiding excessive additions that do not provide proportional benefits. Furthermore, such Sc-modified A356 alloys are particularly relevant for high-performance applications, including aerospace components, electric vehicle structures, and lightweight structural castings, where enhanced mechanical performance and weight reduction justify the increased material cost.

4.5. Heat treatment response and thermal stability of Sc-Containing phases

The response of Sc-modified A356 alloys to T6 heat treatment shows a strong dependence on Sc content and solution-treatment temperature. Compared with the baseline A356.2 alloy, the A356-0.2Sc alloy shows a clear improvement in both YS, UTS and ductility after T6 heat treatment whereas, the A356-0.4Sc alloy displays only a marginal increase in UTS and slight reduction in YS and ductility after T6 heat treatment, compared to the 0.2Sc alloy. However, compared to the baseline A356.2 alloy, it showed marginal improvement in UTS and ductility but slight reduction in YS at the solution temperature of 540 °C and ageing temperature of 170 °C.

The precipitation of fine β''/β'-Mg_2Si phases formed during artificial ageing after solution treatment is the primary source of strengthening in Al-Si-Mg alloys under the T6 condition. Effective age hardening therefore requires (i) adequate dissolution of Mg- and Si-containing phases during solution treatment to achieve a high solute supersaturation in the α-Al matrix, and (ii) controlled precipitation of fine Mg_2Si during ageing. Solution treatment at standard temperatures (540 °C) allows sufficient Mg_2Si dissolution and solute redistribution in the baseline A356.2 alloy and the A356-0.2Sc alloy, resulting in a notable precipitation-strengthening response during ageing.

However, the presence of Sc fundamentally changes this balance. HAADF-STEM imaging and STEM-EDS analyses (Fig. 20) demonstrate that Sc in A356 preferentially forms a thermodynamically stable and coarse Al-Si-Sc based precipitates. The HAADF-STEM image of T6 heat treated A356-0.4Sc alloy (Fig. 20a) shows an individual 60 nm Sc-rich particle embedded within the α-Al matrix. Elemental mapping reveals significant co-enrichment of Sc and Si within the particle, with Mg mainly observed at the particle–matrix interface, and quantitative EDS confirms a composition consistent with the $AlSc_2Si_2$phase. Atomic-resolution HAADF-STEM image, along with corresponding FFT pattern indexed along the [001] zone axis, confirms the tetragonal structure of $AlSc_2Si_2$ rather than the cubic Al_3Sc phase. These particles are semi-coherent to incoherent with the α-Al matrix and significantly coarser (60–160 nm) than strengthening Mg_2Si precipitates. Apart from being coarse, these particles are too sparsely distributed to contribute effectively to precipitation strengthening through shearing or Orowan bypassing. More importantly, they do not dissolve during solution treatment in the temperature range of 500–550 °C. Instead, thermal exposure promotes further coarsening. As a result, the precipitation-hardening response of the A356-0.4Sc alloy is slightly reduced, while that of A356-0.6Sc alloy is significantly diminished compared with the baseline and the A356-0.2Sc alloy. The formation and coarsening of these particles during solution treatment have two detrimental consequences: (1) coarsening reduces the number density of fine, coherent $(Al,Si)_3(Sc,Ti)$ particles that would otherwise contribute to dispersion strengthening; and (2) the formation of $AlSi_2Sc_2$ or $AlSi_2(Sc,Ti)_2$ consumes significant amounts of Si from the α-Al matrix, thereby limiting the Si available for Mg_2Si precipitation during subsequent ageing. Since Mg_2Si is the primary strengthening phase in A356 alloys, this directly suppresses the precipitation-hardening response. This behaviour

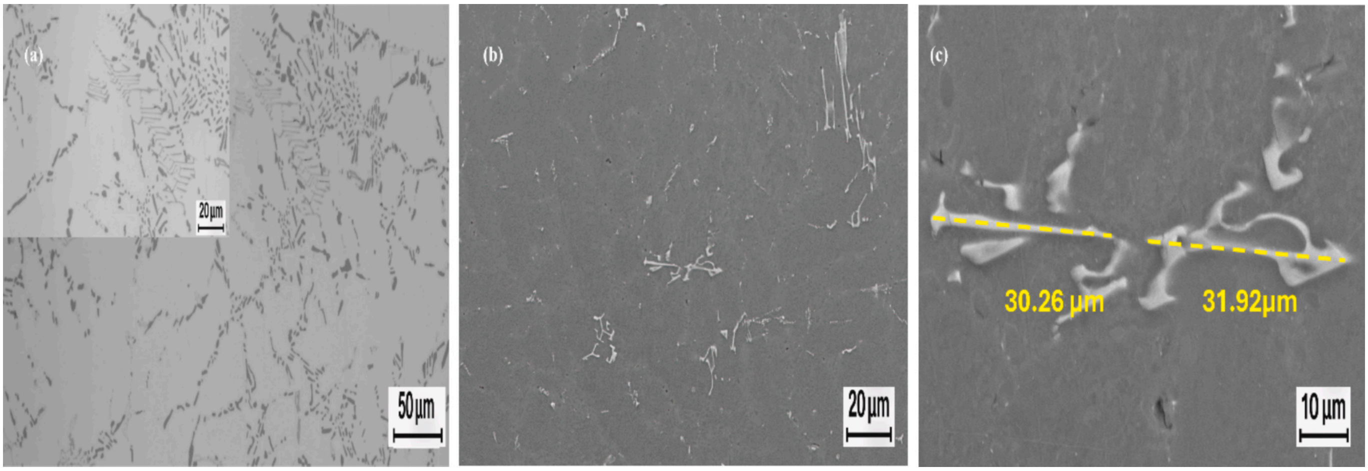

Fig. 19. Microstructural evidence for primary $AlSc_2Si_2$ formation in as-cast A356-0.6Sc alloy showing: (a) Optical micrograph showing coarse Sc-rich intermetallics distributed within the α-Al matrix; (b) SEM BSE image highlighting the spatial distribution of $AlSc_2Si_2$ particles; and (c) High-magnification SEM BSE image showing elongated primary $AlSc_2Si_2$ particles with characteristic lengths of 30–32 μm.

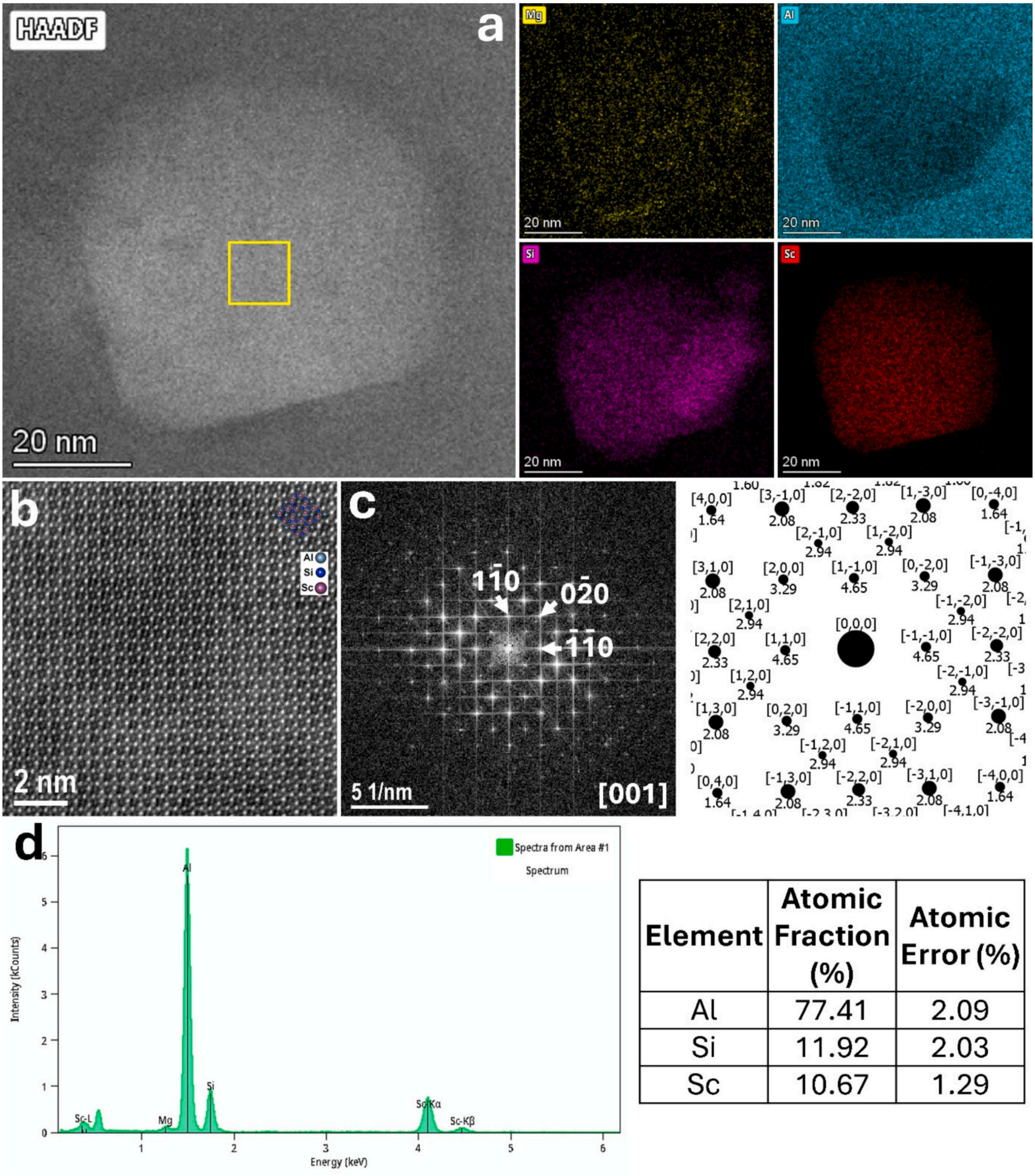

Element	Atomic Fraction (%)	Atomic Error (%)
Al	77.41	2.09
Si	11.92	2.03
Sc	10.67	1.29

Fig. 20. STEM characterisation of the Sc-containing intermetallic phase in T6-treated A356-0.4Sc alloy: (a) HAADF-STEM image showing an individual ~ 60 nm Sc-rich particle within the α-Al matrix. The corresponding STEM-EDS elemental maps reveal strong co-enrichment of Sc and Si within the particle, while Mg is predominantly observed around the particle, likely associated with Mg_2Si formation at the particle–matrix interface; (b) atomic-resolution HAADF-STEM image displaying well-ordered atomic arrangement characteristic of the $AlSc_2Si_2$ phase; (c) FFT pattern indexed along the [001] zone axis, showing reflections consistent with the tetragonal $AlSc_2Si_2$ structure, together with the simulated diffraction pattern for comparison; and (d) EDS spectrum extracted from the yellow highlighted region, confirming the presence of Mg, Al, Si and Sc.

contrasts sharply with wrought Al–Sc alloys, in which coherent $L1_2$ Al_3Sc precipitates dissolve during solution treatment and re-precipitate as fine nanoscale strengthening particles during ageing.

As proposed by Dumbre et al. [46], the transient Al_3Sc or $(Al,Si)_3Sc$-type nanoscale clusters formed during early solidification or rapid cooling are unstable during prolonged exposure at solution-treatment temperatures. During solution treatment, Sc diffuses and reacts with Si (and Ti, where present), leading to the transformation and coarsening of these clusters into $AlSc_2Si_2$ type phases. Similar coarsening behaviour has been reported for Al-Si-Zr-Ti systems, where Al_3Zr is replaced by more stable $Al_3(Si, Zr)$ or $(Al, Si)_3(Zr, Ti)$ phases during heat treatment, leading to limited precipitation strengthening despite excellent thermal stability [58].

Lowering the solution-treatment temperature was therefore explored as a potential strategy to suppress the coarsening of Sc-rich intermetallics and the precipitates formed during the heat treatment. Solution treatments at 500–520 °C and were found to effectively limit coarsening of Al-Si-Sc-(Ti) phases; however, these temperatures were insufficient to fully dissolve Mg_2Si and homogenise the matrix, leading to an inadequate supersaturation of Mg and Si and a correspondingly poor age-hardening response. Conversely, higher solution-treatment temperatures (≥540 °C) promoted Mg_2Si dissolution but accelerated the coarsening of Sc-containing intermetallics, negating the benefits of precipitation strengthening. To address this trade-off, a series of two-step solution treatments combining a low-temperature step (500–520 °C) followed by a higher-temperature step (530–545 °C) were also explored during the study. Despite these efforts, no significant improvement in the age-hardening response was achieved compared with the conventional T6 treatment, indicating that the intrinsic thermal stability of the Al-Si-Sc-(Ti) phases dominates the solution-treatment behaviour.

Among the conditions examined, a solution-treatment temperature of approximately 535 °C was found to provide the best trade-off between strength and ductility for the A356-0.4Sc and A356-0.6Sc alloys. At this temperature, complete Mg_2Si dissolution is achieved while limiting excessive coarsening of Sc-rich intermetallics, resulting in significant improvement of ductility and UTS but deterioration in YS. Consequently, this temperature was selected as the optimum solution-treatment condition for the higher-Sc alloys in the present study.

Overall, these results demonstrate that the reduced heat-treatment response of Sc-rich A356 alloys is not caused by insufficient ageing kinetics but rather by the thermodynamic stability and coarsening behaviour of Al-Si-Sc-(Ti) precipitates during solution treatment. This finding highlights a fundamental limitation of high Sc additions in Al-Si-Mg cast alloys and underscores the existence of an optimum Sc content, beyond which further additions are detrimental to precipitation strengthening and mechanical performance.

5. Conclusions

Based on a combined thermodynamic, microstructural, thermal, and mechanical investigation of Sc-modified A356 cast alloys, the following conclusions can be drawn:

1. Sc additions up to 0.4 wt% significantly enhance the mechanical properties in as-cast condition by promoting multi-scale microstructural refinement. Compared to the baseline A356.2 alloy, the A356-0.4Sc alloy shows about 52% reduction in α-Al grain size, around 19% reduction in SDAS, transformation of eutectic Si from acicular to fibrous morphology, and refinement of Fe-bearing intermetallics, resulting in a simultaneous increase in YS, UTS and elongation.
2. The strengthening of Sc-modified alloys arises from the synergistic contribution of multiple mechanisms, including Hall-Petch grain-boundary strengthening, SDAS-driven microsegregation suppression, eutectic Si and Fe-intermetallic morphology modification, and dispersion strengthening by nanoscale Al-Si-Sc-(Ti) dispersoids.
3. Conventional T6 heat treatment is progressively less effective with increasing Sc content, as thermodynamically stable $AlSi_2\ (Sc, Ti)_2$ based intermetallics formed during solidification do not dissolve during solution treatment (500–550 °C) but instead coarsen. Furthermore, the precipitates formed during the heat treatment process are also coarse (60–160 nm) which leads to a reduced age-hardening response, particularly in alloys containing $\geq$ 0.4 wt% Sc.
4. An optimum Sc addition window of 0.2–0.4 wt% is established for A356 alloys, beyond which ($>$ 0.52 wt% Sc) primary $AlSc_2Si_2$ forms early during solidification, consuming Sc and Si, producing coarse intermetallics, and degrading both as-cast and heat-treated properties. This study thus provides a clear alloy-design guideline for Sc-modified A356 cast alloys, reconciling previously inconsistent literature reports.

CRediT authorship contribution statement

Priyansh Khandelwal: Writing – original draft, Methodology, Investigation, Formal analysis, Data curation, Conceptualization. **Raluca Florentina Negrea:** Writing – review & editing, Validation, Methodology, Formal analysis, Data curation. **Jason Nunn:** Writing – review & editing, Supervision, Project administration. **Scott Honan:** Supervision, Project administration, Funding acquisition. **Shouxun Ji:** Writing – review & editing, Visualization, Validation, Supervision, Methodology, Funding acquisition, Conceptualization.

Declaration of competing interest

The authors declare that they have no known competing financial interests or personal relationships that could have appeared to influence the work reported in this paper.

Acknowledgements

This research was funded the Engineering and Physical Sciences Research Council (EPSRC) under project UKRI1682 and Innovate UK (IUK) under grant number APC 10113213. Priyansh Khandelwal would like to acknowledge Niocorp Developments Limited, USA for their support. The authors would like to acknowledge the use of the BCAST Advanced Characterisation Suite (BACS) set up through the funding received from UKRI Infrastructure grant: entitled “Future Metallurgy Centre”.

Appendix A. Supplementary data

Supplementary data to this article can be found online at https://doi.org/10.1016/j.matdes.2026.116184.

Data availability

Data will be made available on request.

References

[1] J.G. Kaufman, Introduction to aluminum alloys and tempers. ASM, International (2000) 258 p.
[2] D.JR. Alloying, Understanding the Basics. (2001), https://doi.org/10.1361/autb2001p351. Available at:.
[3] J.A. Taylor, Iron-containing intermetallic phases in Al-Si based casting alloys, Procedia Mater. Sci. Elsevier BV 1 (2012) 19–33, https://doi.org/10.1016/j.mspro.2012.06.004. Available at:.
[4] B.S. Murty, S.A. Kori, M. Chakraborty, Grain refinement of aluminium and its alloys by heterogeneous nucleation and alloying international materials reviews, IOM Communications Ltd. (2002) 3–29, https://doi.org/10.1179/095066001225001049. Available at:.

[5] Gezer BT., Toptan F., Daglilar S., Kerti I. Production of Al-Ti-C grain refiners with the addition of elemental carbon. Materials and Design. June 2010; 31(SUPPL. 1). Available at: DOI:10.1016/j.matdes.2009.09.002.

[6] A.L. Greer, P.S. Cooper, M.W. Meredith, W. Schneider, P. Schumacher, J.A. Spittle, et al., Grain refinement of aluminium alloys by inoculation, Adv. Eng. Mater. Wiley-VCH Verlag (2003) 81–91, https://doi.org/10.1002/adem.200390013. Available at:.

[7] Nowak M., Bolzoni L., Hari Babu N. Grain refinement of Al-Si alloys by Nb-B inoculation. Part I: Concept development and effect on binary alloys. Materials and Design. Elsevier Ltd; 5 February 2015; 66(PA): 366–375. Available at: DOI: 10.1016/j.matdes.2014.08.066.

[8] Easton M., Stjohn D. Grain Refinement of Aluminum Alloys: Part I. The Nucleant and Solute Paradigms-A Review of the Literature.

[9] Fan Z., Wang Y., Zhang Y., Qin T., Zhou XR., Thompson GE., et al. Grain refining mechanism in the Al/Al-Ti-B system. Acta Materialia. Elsevier Ltd; 1 February 2015; 84: 292–304. Available at: DOI:10.1016/j.actamat.2014.10.055.

[10] A.K. Dahle, K. Nogita, S.D. McDonald, C. Dinnis, L. Lu, Eutectic modification and microstructure development in Al-Si Alloys, Mater. Sci. Eng.: A. Elsevier BV 15 (413–414) (2005) 243–248, https://doi.org/10.1016/j.msea.2005.09.055. Available at:.

[11] S.-Z. Lu, A. Hellawell, The mechanism of silicon modification in aluminum-silicon alloys: Impurity induced twinning, Metall. Trans. A 18 (10) (1987) 1721–1733, https://doi.org/10.1007/BF02646204. Available at:.

[12] Moniri S., Xiao X., Shahani AJ. The mechanism of eutectic modification by trace impurities. Scientific Reports. Nature Publishing Group; 1 December 2019; 9(1). Available at: DOI:10.1038/s41598-019-40455-3.

[13] D. Emadi, J.E. Gruzleski, J.M. Toguri, The effect of na and Sr modification on surface tension and volumetric shrinkage of A356 alloy and their influence on porosity formation, Metall. Trans. B 24 (6) (1993) 1055–1063, https://doi.org/10.1007/BF02660997. Available at:.

[14] Wang B., Wang J., Liu X., Li Q., Liu X. Uncovering the effects of neutralizing elements (Co, Mn and Cr) on the Fe-rich intermetallic formation in Al–Si–Cu alloys. Materials Science and Engineering: A. Elsevier Ltd; 14 November 2022; 858. Available at: DOI:10.1016/j.msea.2022.144090.

[15] Ji S., Yang W., Gao F., Watson D., Fan Z. Effect of iron on the microstructure and mechanical property of Al-Mg-Si-Mn and Al-Mg-Si diecast alloys. Materials Science and Engineering: A. Elsevier Ltd; 1 March 2013; 564: 130–139. Available at: DOI: 10.1016/j.msea.2012.11.095.

[16] Shabestari SG. The effect of iron and manganese on the formation of intermetallic compounds in aluminum-silicon alloys. Materials Science and Engineering: A. Elsevier BV; 15 October 2004; 383(2): 289–298. Available at: DOI:10.1016/j.msea.2004.06.022.

[17] Limmaneevichitr C., Eidhed W. Fading mechanism of grain refinement of aluminum-silicon alloy with Al-Ti-B grain refiners. Materials Science and Engineering: A. Elsevier BV; 25 May 2003; 349(1–2): 197–206. Available at: DOI: 10.1016/S0921-5093(02)00751-7.

[18] Wang Y., Que Z., Hashimoto T., Zhou X., Fan Z. Mechanism for Si Poisoning of Al-Ti-B Grain Refiners in Al Alloys. Metallurgical and Materials Transactions A: Physical Metallurgy and Materials Science. Springer; 1 November 2020; 51(11): 5743–5757. Available at: DOI:10.1007/s11661-020-05950-7.

[19] Liu L., Samuel AM., Samuel FH., Doty HW., Valtierra S. Influence of oxides on porosity formation in Sr-treated Al-Si casting alloys.

[20] Lu S-Z., Hellawell A. Modification of Al-Si alloys: Microstructure, thermal analysis, and mechanisms. JOM. February 1995; 47(2): 38–40. Available at: DOI:10.1007/BF03221405.

[21] Dietrich BG., Becker H., Smolka M., Keßler A., Leineweber A., Wolf G. Intermetallic Sludge Formation in Fe Containing Secondary Al–Si Alloys Influenced by Cr and Mn as Preparative Tool for Metal Melt Filtration. Advanced Engineering Materials. 9 September 2017; 19(9). Available at: DOI:10.1002/adem.201700161.

[22] N.A. Belov, D.G. Eskin, A.A. Aksenov, Alloys with transition metals multicomponent phase diagrams, Elsevier (2005) 287–340, https://doi.org/10.1016/B978-008044537-3/50009-3. Available at:.

[23] Zakharov V V. About Alloying of Aluminum Alloys with Transition Metals. Metal Science and Heat Treatment. Springer New York LLC; 1 May 2017; 59(1–2): 67–71. Available at: DOI:10.1007/s11041-017-0104-2.

[24] Knipling KE., Dunand DC., Seidman DN. Criteria for developing castable, creep-resistant aluminum-based alloys-A review. 2006. Available at: www.ijmr.de.

[25] Marquis EA., Seidman DN., Marquis EA., Seidman DN. Nanoscale structural evolution of Al3Sc precipitates in Al (Sc) alloys NANOSCALE STRUCTURAL EVOLUTION OF Al 3 Sc PRECIPITATES IN Al(Sc) ALLOYS. Acta mater. 2001. Available at: www.elsevier.com/locate/actamat.

[26] Test Methods for Tension Testing of Metallic Materials. West Conshohocken, PA: ASTM International; 2025. Available at: DOI:10.1520/E0008_E0008M-25.

[27] Deng Y., Zeng G., Xian J., Zhan H., Liu C., Gourlay CM. Eutectic intermetallic formation during solidification of a Mg-Sn-Al-Zn-Mn alloy. Materials Characterization. Elsevier Inc.; 1 April 2022; 186. Available at: DOI:10.1016/j.matchar.2022.111807.

[28] Guo Z., Liu X., Xue J. Fabrication of Al-Si-Sc alloy bearing AlSi2Sc2 phase using ultrasonically assisted molten salt electrolysis. Journal of Alloys and Compounds. Elsevier Ltd; 15 August 2019; 797: 883–889. Available at: DOI:10.1016/j.jallcom.2019.05.133.

[29] Xu SP., Shi CS., Zhao NQ., He CN. Microstructure and tensile properties of A356 alloy with different Sc/Zr additions. Rare Metals. University of Science and Technology Beijing; 1 September 2021; 40(9): 2514–2522. Available at: DOI: 10.1007/s12598-020-01529-8.

[30] A. Masita, W.H. Yeo, L.H. Saw, Y.P. Lim, J.W. Lee, T.C. Ng, in: Mechanical and Fatigue Properties of Gravity Die-Cast A356 Aluminium Alloy with Addition of Scandium, Institute of Physics Publishing, 2019, https://doi.org/10.1088/1755-1315/268/1/012059.

[31] Pramod SL., Ravikirana., Rao AKP., Murty BS., Bakshi SR. Effect of Sc addition and T6 aging treatment on the microstructure modification and mechanical properties of A356 alloy. Materials Science and Engineering: A. Elsevier; 2016; 674: 438–450. Available at: DOI:10.1016/j.msea.2016.08.022.

[32] Y.P. Lim, W.H. Yeo, A. Masita, Effect of heat treatment on gravity die-cast Sc-A356 aluminium alloy. Manufacturing Review. EDP, Sciences 4 (2017), https://doi.org/10.1051/mfreview/2017003. Available at:.

[33] Lu Z., Zhang L. Thermodynamic description of the quaternary Al-Si-Mg-Sc system and its application to the design of novel Sc-additional A356 alloys. Materials and Design. Elsevier Ltd; 15 February 2017; 116: 427–437. Available at: DOI:10.1016/j.matdes.2016.12.034.

[34] P. Pandee, C.M. Gourlay, S.A. Belyakov, U. Patakham, G. Zeng, C. Limmaneevichitr, AlSi2Sc2 intermetallic formation in Al-7Si-0.3Mg-xSc alloys and their effects on as-cast properties, J. Alloys Compounds. Elsevier B.v. 731 (2018) 1159–1170, https://doi.org/10.1016/j.jallcom.2017.10.125. Available at:.

[35] Muhammad A., Xu C., Xuejiao W., Hanada S., Yamagata H., Hao LR., et al. High strength aluminum cast alloy: A Sc modification of a standard Al-Si-Mg cast alloy. Materials Science and Engineering: A. Elsevier Ltd; 16 May 2014; 604: 122–126. Available at: DOI:10.1016/j.msea.2014.03.005.

[36] Xu C., Xiao W., Zheng R., Hanada S., Yamagata H., Ma C. The synergic effects of Sc and Zr on the microstructure and mechanical properties of Al-Si-Mg alloy. Materials and Design. Elsevier Ltd; 25 December 2015; 88: 485–492. Available at: DOI:10.1016/j.matdes.2015.09.045.

[37] P. Pandee, C.M. Gourlay, S.A. Belyakov, R. Ozaki, H. Yasuda, C. Limmaneevichitr, Eutectic morphology of Al-7Si-0.3Mg alloys with scandium additions, in: Metall. Mater. Trans. A: Phys. Metall. Mater. Sci., 45, Springer Boston, 2014, pp. 4549–4560, https://doi.org/10.1007/s11661-014-2395-x.

[38] Kaiser MS., W Kurny AS. EFFECT OF SCANDIUM ON THE GRAIN REFINING AND AGEING BEHAVIOUR OFCASTAl-Si-MgALLOY. 2011.

[39] Zhang Z., Zhao Q., Liu L., Xia X., Zheng C., Quan L., et al. Mechanical performances of Al-Si-Mg alloy with dilute Sc and Sr elements. Materials. MDPI AG; 1 February 2020; 13(3). Available at: DOI:10.3390/ma13030665.

[40] Batsanov ss., The atomic radii of the elements, Russ. J. Inorg. Chem. 36 (12) (1991) 1694–1706.

[41] H. Mao, P. Lian, Q. Wei, Y. Wang, H. Xu, Y. Li, Effect of scandium on grain refinement mechanism and mechanical properties of Al–7Si–0.6 Mg alloy at different cooling rates, J. Mater. Res. Technol. 26 (2023) 4784–4796, https://doi.org/10.1016/j.jmrt.2023.08.227. Available at:.

[42] Castillo-Sánchez JR., Salloum-Abou-Jaoude G., Gheribi AE., Lafaye P., Oishi K., Masse JP., et al. Synthesis and characterization of (Al,Si)3(Zr,Ti)-D022/D023 intermetallics: Understanding the stability of silicon substitution. Acta Materialia. Acta Materialia Inc; 1 January 2024; 262. Available at: DOI:10.1016/j.actamat.2023.119455.

[43] Chen D., Chen Z., Wu Y., Wang M., Ma N., Wang H. First-principles investigation of mechanical, electronic and optical properties of Al3Sc intermetallic compound under pressure. Computational Materials Science. Elsevier; 2014; 91: 165–172. Available at: DOI:10.1016/j.commatsci.2014.05.007.

[44] Wang Z., Liu X., Zhu C., Xue J., Guo Z., Zhang Y., et al. Influence of the interaction between Si and Sc on the microstructure and tensile properties of as casted Al-Si-Sc alloys. Journal of Alloys and Compounds. Elsevier Ltd; 15 January 2023; 932. Available at: DOI:10.1016/j.jallcom.2022.167650.

[45] Xiang L xin., Dong D., Gu G chao., Lu Y peng., Zheng H liang. AlSi2(Sc, Zr, Ti)2 phase formation in Sc(Zr)-containing Al–7Si–Mg alloy and their effects on microstructure and mechanical properties. Journal of Materials Research and Technology. Elsevier Editora Ltda; 1 January 2026; 40: 165–175. Available at: DOI: 10.1016/j.jmrt.2025.12.066.

[46] Dumbre J., Kairy SK., Anber E., Langan T., Taheri ML., Dorin T., et al. Understanding the formation of (Al,Si)3Sc and V-phase (AlSc2Si2) in Al-Si-Sc alloys via ex situ heat treatments and in situ transmission electron microscopy studies. Journal of Alloys and Compounds. Elsevier Ltd; 25 April 2021; 861. Available at: DOI:10.1016/j.jallcom.2020.158511.

[47] W. Prukkanon, N. Srisukhumbowornchai, C. Limmaneevichitr, Modification of hypoeutectic Al-Si alloys with scandium, J. Alloy. Compd. 477 (1–2) (2009) 454–460, https://doi.org/10.1016/j.jallcom.2008.10.016. Available at:.

[48] U. Patakham, J. Kajornchaiyakul, C. Limmaneevichitr, Modification mechanism of eutectic silicon in Al-6Si-0.3Mg alloy with scandium, J. Alloys Compounds. Elsevier Ltd 575 (2013) 273–284, https://doi.org/10.1016/j.jallcom.2013.05.139. Available at:.

[49] Xu C., Xiao W., Hanada S., Yamagata H., Ma C. The effect of scandium addition on microstructure and mechanical properties of Al-Si-Mg alloy: A multi-refinement modifier. Materials Characterization. Elsevier Inc.; 1 December 2015; 110: 160–169. Available at: DOI:10.1016/j.matchar.2015.10.030.

[50] Wang Y., Zhao X., Liu F., Hou X., Bai P., Cui X. Modification mechanism of eutectic Si phases in Al-Si-Mg series alloys with Sc addition. Journal of Alloys and Compounds. Elsevier Ltd; 20 July 2025; 1036. Available at: DOI:10.1016/j.jallcom.2025.181912.

[51] Shabestari SG., Ghodrat S. Assessment of modification and formation of intermetallic compounds in aluminum alloy using thermal analysis. Materials Science and Engineering: A. Elsevier BV; 15 October 2007; 467(1–2): 150–158. Available at: DOI:10.1016/j.msea.2007.05.022.

[52] Y.C. Tzeng, C.T. Wu, H.Y. Bor, J.L. Horng, M.L. Tsai, S.L. Lee, Effects of scandium addition on iron-bearing phases and tensile properties of Al-7Si-0.6Mg alloys,

Mater. Sci. Eng.: A. Elsevier 593 (2014) 103–110, https://doi.org/10.1016/j.msea.2013.11.039. Available at:.

[53] Zhang W., Liu Y., Yang J., Dang J., Xu H., Du Z. Effects of Sc content on the microstructure of As-Cast Al-7 wt.% Si alloys. Materials Characterization. April 2012; 66: 104–110. Available at: DOI:10.1016/j.matchar.2011.11.005.

[54] Hall EO. The Deformation and Ageing of Mild Steel: III Discussion of Results. Proceedings of the Physical Society. Section B. 1 September 1951; 64(9): 747–753. Available at: DOI:10.1088/0370-1301/64/9/303.

[55] N.J. Petch, The cleavage strength of polycrystals, J. Iron Steel Inst. 174 (1953) 25–28, https://doi.org/10.1016/0013-7944(87)90050-6. Available at:.

[56] Nie JF., Morton AJ., Muddle BC., Easton M., Wang H., Grandfield J., et al. An Analysis of the Effect of Grain Refinement on the Hot Tearing of Aluminium Alloys CRC for Cast Metals Manufacturing (CAST). 2004.

[57] Kendig KL., Miracle DB. Strengthening mechanisms of an Al-Mg-Sc-Zr alloy. Acta Materialia. 2002. Available at: www.actamat-journals.com.

[58] Rahimian M., Amirkhanlou S., Blake P., Ji S. Nanoscale Zr-containing precipitates; a solution for significant improvement of high-temperature strength in Al-Si-Cu-Mg alloys. Materials Science and Engineering: A. Elsevier Ltd; 4 April 2018; 721: 328–338. Available at: DOI:10.1016/j.msea.2018.02.060.